Experimental implementation of third-order nonlinear infrared spectroelectrochemistry

William Robert Miller

A dissertation

submitted in partial fulfillment of the

requirements for the degree of

Doctor of Philosophy

University of Washington

2023

Reading Committee:

Munira Khalil, Chair

Joshua Vaughan

Cody Schlenker

Program Authorized to Offer Degree:

Chemistry

University of Washington

Abstract

Experimental implementation of third-order nonlinear infrared spectroelectrochemistry

William Robert Miller

Chair of the Supervisory Committee:
Professor Munira Khalil
Chemistry

Infrared (IR) spectroelectrochemistry (SEC) is a field with both established and emerging techniques. This work presents a broadly applicable and extensively modular IR-SEC design that's specialized for laser table experiments, but also functional on some tabletop spectrometers. This work demonstrates the electrochemical and spectroscopic viability of this cell in a transmissive FTIR spectrometer using $Fe^{II\backslash III}(CN)_6^{4-\backslash 3-}$ as a benchmark, and then realizes its laser table SEC experiment ability through pump-probe IR and two-dimensional (2D) IR SEC demonstrations with $Fe_6^{III}(CN)_6^{3-}$ as an analyte. The SEC infrastructure works entirely as intended, although data presented here shows that additional care should be taken to reduce scattering when measuring weakly absorbing signals. The primary focus of this work is put into

cataloguing minute details of the setup, maintenance, and standard operating procedures to facilitate future work.

TABLE OF CONTENTS

LIST OF FIGURES

LIST OF TABLES

DEDICATION

I'm dedicating this to my colleagues, friends, and the community of people I found here who kept me afloat when I was sinking. It's only cliché because it's true – I would not have made it this far without them!

Chapter 1. INTRODUCTION

While the importance of novel scientific discovery and its subsequent application into ground-breaking analytical techniques is the essential beginning of any field or sub-field of study, these analytical techniques often cascade into scientific advances in other fields of study. These can eventually evolve into engineering and public initiatives, but usually only when these ground-breaking techniques are eventually made more accessible. Techniques like "polarography" (or more contemporarily called voltammetry) began as novel and obscure, but upon widespread adoption became integral to electrochemical analysis that's studied in many different sub-fields of chemistry and biology[1–3] ranging from chemical catalysis and kinetics to quantification of glucose in medical blood samples. It wouldn't be an overstatement to suggest that the process of facilitating an analytical technique for non-specialists to the field that originally spawned that technique is incredibly important for advancing scientific progress as a whole. Sometimes, the process of facilitating these analytical techniques isn't even an issue of advancing technology, but to just provide the fruits of previous work freely and reliably and save precious time for others.

1.1 More Degrees of Freedom

Spectroelectrochemistry (SEC) is a great point for exactly this phenomenon. The technique first established by Dr. Theodore Kuwana in 1964 as largely a proof of concept, using electrically conductive glass to simultaneously perform electrochemistry and measure the absorbance changes during electrolysis of electroactive species in solution[4]. By 1989, this technique had been extended to most of the electromagnetic (EM) spectrum with a plurality of different infrastructural designs[5] and this interest has only accelerated further as SEC proves increasingly useful for studying catalysts, biomolecules, and photoelectric materials[6–14] of recent increasing interest. It's worth

noting that despite this rapid expansion of the scope of SEC experiments, IR-SEC methodology was comparatively lacking by 1989 due to the inherent difficulties of consolidating electrochemical experiments and infrared (IR) measurements. Many foundational SEC experiments were made using conductive glass that was transparent to the EM spectrum used, but electrically conductive materials are implicitly IR reflective. Aqueous solutions popular with many spectroscopic techniques involve large amounts of IR background absorption. These solvent considerations can also impose additional design issues that introduce problems for general use, such as ensuring the construction is inert to the solution yet spectrally transparent, the need for adjustable spectral path length, and extremely specialized and expensive components. As such, SEC, and IR SEC especially, has always been a technique whose generalizability has always been hampered by the need for specialized infrastructure, with the greatest focal piece being the need for an optically transmissive sample holder capable of performing electrochemistry at the site of spectral transmission. In contemporary literature, these are usually referred to as SEC cells[5,11,15,16]. Despite IR SEC's lagging progress compared to other SEC techniques, commercial IR SEC cells for use with transmissive linear IR spectrometers are available for many applications, although most of them are optically transmissive thin layer electrode (OTTLE) cells. These work by placing the electrochemical components of the SEC cell (usually a set of thin metal wires or wire meshes) between two CaF_2 glass panes. This means that OTTLE cells have their spectral path length fundamentally set to the thickness of the wires or meshes used for their electrochemical components. Still, this isn't always an issue for SEC cells and these commercially available OTTLE cells work well for use in most benchtop IR spectrometers.

The increasing ease of performing IR SEC experiments is important, as IR SEC is a powerful technique. Electrochemistry has long been an important method for studying reaction kinetics and

electronically active materials[7,17,18], where holding and changing the oxidation state of a catalyst or electronically unique molecule can allow the researcher to measure chemical intermediates and/or the unique electronic properties of a molecule. IR spectroscopy is classically useful for probing the vibrations of the analyte molecule's bonds, which report of the electronic and geometric character of those bonds. Thus, the attractive prospect of IR SEC is adjusting the oxidation state of an analyte and probing the resulting changes to the geometry and electronic character of various bonds of the analyte molecule via IR spectroscopy. These insights can be used to study and determine or study reactivity[6,7], or to study molecular electronic delocalization[19,20], or even simply to understand the molecular connections between the electronic and vibrational properties of a molecule more broadly.

1.2 The Need for a Customized SEC Cell

Optically transmissive thin layer electrode (OTTLE) SEC cells can be purchased for all kinds of linear SEC. In general, these work well for linear spectroscopies that don't need to consider laser beam scattering or considerable IR absorption. However, this criterion is not tenable for any ultrafast IR spectroscopy technique. Non-OTTLE cells are not regularly sold, so anyone looking to do third-order or other nonlinear spectroscopy need to design their own SEC cells[9,15,16,21–23]. This can be a large part of the reason why nonlinear SEC experiments are much rarer than linear SEC experiments with readily available and standardized equipment[5–7,19,20]. This is also why so many SEC cell designs are highly specific rather than being standardized for general use or a commercial model being available.

As mentioned before, IR SEC infrastructure generally lags behind other SEC infrastructure because of some of the specific issues with IR SEC, and this is somewhat compounded for nonlinear IR SEC. One thing that makes doing nonlinear IR SEC is that the highly customized

devices that are published are often designed with highly specific or expensive parts that are difficult to acquire[15,16,21–24] often because the parts in question are essential to the device functioning but aren't sold anymore, or because the customized part is inordinately expensive for use by non-specialists. Thus, not only are there no standardized or commercially available designs for nonlinear SEC cells, but even trying to replicate a published design is often not possible.

This is why one sub-goal accomplished in this work is to make all design files and a bill of materials for the construction of the realized SEC cell easily and freely accessible. While the design specified here can't completely eschew customized construction, the most advanced equipment required are metal and plastic machining equipment (this design's custom body and mounted parts were made with CNC machines) and a sputter coating device, which are frequently found in nanofabrication facilities. Additionally, the design of this SEC cell is intentionally modular and relatively simple, such that it's not difficult to modify the device and use replacement parts if any of the purchased parts from the bill of materials is no longer available or if the user desires additional functionality.

1.3 Construction, Testing, and Thesis Organization

This thesis describes the design, construction, and testing of the aforementioned SEC cell. The functioning of the SEC cell was first proven to work using a benchtop FTIR spectrometer SEC test, then its nonlinear SEC capabilities are demonstrated with a PPIR SEC test and a 2DIR SEC test. These details are spread across the following chapters 2 through 6.

First, in Chapter 2, the construction of the SEC flow cell and its major components is described. This chapter is dedicated to how each piece of the SEC cell is acquired or constructed. The chapter concludes with a bill of purchase-able materials.

Chapter 3 describes the usage and maintenance of the SEC cell. This chapter walks through every part of typically using the SEC cell, including walking through using the computer GUI's required to operate the SEC components. Chapter 3 walks through setting up the SEC cell, and standard operating procedures for its electrochemical infrastructure. This chapter also includes some noteworthy trouble shooting advice for users with less familiarity with electrochemistry, and concludes with the setup details and resulting data of an FTIR SEC test using an aqueous solution of 40mM $K_3Fe(CN)_6$ in 1M KNO_3. Some of the timed FTIR SEC tests of this solution inform general SEC procedures, and discussed in that section.

Chapter 4 starts by describing the laser table infrastructure, and goes into detail on standard operating procedures to set up the unique parts of the PPIR or 2DIR infrastructure. This chapter concludes by going into detail on how to use the various labview GUI's necessary to set up and run PPIR and 2DIR experiments.

Chapter 5 features the PPIR SEC test on a 10mM $K_3Fe(CN)_6$ and 1M KNO_3 in formamide solution. The data and analysis are briefly described, and conclusions are made about the SEC cell's performance and how it might be improved. Chapter 6 describes the same discussions and analysis but for a 2DIR SEC test on that same solution.

Chapter 2. SEC FLOW CELL CONSTRUCTION

This chapter outlines the overall composition of the cell, and provides instructions on constructing the sample holder, replacing broken parts, and assembling it for use. There are two configurations currently designed for the cell – one design for temperature control and one without temperature control. While most of the physical components for temperature control are present, the operating

infrastructure for the temperature control was never implemented. Still, the physical components will be outlined here to assist anyone who'd seek to implement it.

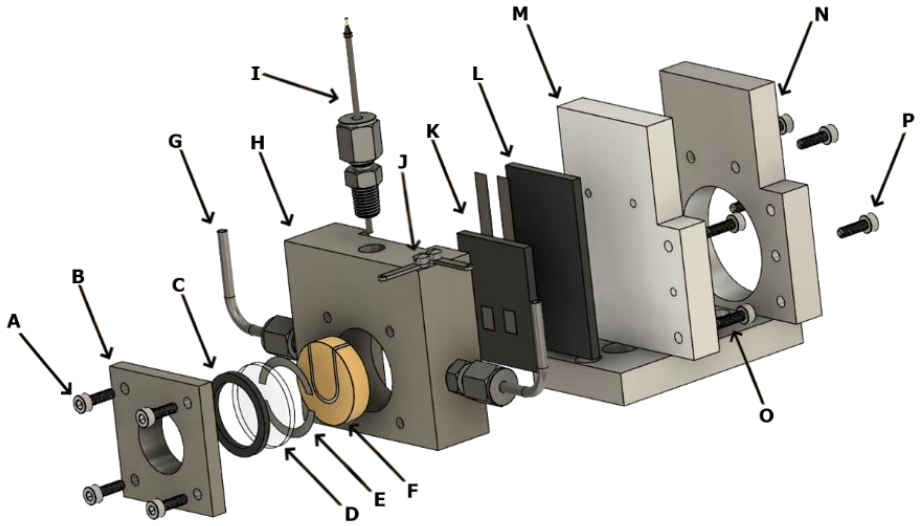

Figure 2.1. CAD drawing of the configuration for the flow cell as used in this work. A) M3x0.5x10mm screws for the front cover; B) front cover plate with 20mm aperture; C) 1" outer-diameter front VITON gasket; D) 2mm thick CaF_2 window; E) 25μm thick PTFE (Teflon) spacers; F) mirror-electrode piece; G) collective flow tubing; H) plastic body for the cell, featuring its 1" ME slot; I) reference electrode apparatus inside its Yor-Lok tube-to-pipe adapter housing; J) ring mounts to which (not shown) wires are soldered to the tin-foil contacts; K) VITON back gasket featuring a slit cut for Sn-foil contacts; L) secondary VITON or Si rubber gasket which fills the rest of the space between the previous cell pieces, compressing them; M) cell back (no hole); N) table mount; O) M3x0.5x10mm screws that screw the cell back to the cell body, P) M4x0.5x10mm screws that screw the table mount to the cell back.

2.1 Making the Cell Body and Front Cover

The cell's front cover (Figure 2.1, B) is made of polyetheretherketone (PEEK) plastic, a plastic known for its relatively chemical and thermally inert properties. Most notably, its glass transition temperature is at 143^oC, and its melting temperature is at 343^oC[25]. It's additionally resistant to

degradation in both aqueous and organic solvents, although it can be degraded by elemental halogens and strong Bronsted and Lewis acids[25]. None of the work done here has ever degraded the plastic body or cover of the cell.

The body (Figure 2.1, H) was originally designed via the SolidWorks CAD design software, but later transitioned to Fusion360. The body is summarily a block of PEEK plastic with four M3 screw holes in the front and back, one central cylindrical hole, three 1/16" NPT pipe thread holes on the tops and sides with an additional fluid flow hole that connects to the central hole, and a groove at the back for gaskets. The M3 screw holes were originally reinforced with a metal spring (Helicoil) to reinforce the thread, but this did not hold out. A much more reliable means of anchoring the screws was to embed a piece of threaded aluminum into the PEEK body with the M3 thread, as currently implemented.

The front cover is also made of PEEK plastic, and is likewise designed via SolidWorks CAD software. It's summarily a flat square with four holes for M3 screws and a 1" cylindrical extrusion on the back. Through the center of the square, and the extrusion, is the cylindrical hole for the beam.

These parts are ideally constructed by a professional with a Computer Numerical Control manufacturing machine.

2.2 Making the Back Plate and Table Mount

The table mount (Figure 2.1, N) and the back plate (Figure 2.1, M) for the cell are both made of aluminum. These pieces are made with stock aluminum, since their only structural consideration is to be sturdy and cost-efficient. The table mount is a flat plate with holes for M3 screws for the back of the cell or M4 screws for the back plate. Additionally, the table mount has two sets of screw holes on a bottom plate that extends from the back in an "L" shape. These four screw holes

are two screw holes two ¼”-20 screws and two #8-32 screws, which serve to fasten the table mount to a variety of potential mounting sites on either a laser table or on optic posts.

2.3 MAKING THE VITON GASKETS

The SEC cell features three types of rubber gaskets that are made with 1/8” thick Viton™ fluoroelastomer rubber, sheets of which are supplied by McMasterCarr supply co. (Prod.ID#86075K24) and cut by hand.

For the front gasket that buffers between the front CaF_2 windows and the PEEK front cover (Figure 2.1, C), the circular shape is first cut out using a 1” hole cutter, then the interior of the circle is cut into an inner circle until the result is a cylindrical ring with an approximately 3mm thick diameter thickness.

The back-most Viton™ gasket is cut about 60mm in length, and then cut to the width of the groove it will sit within, about 30mm (Figure 2.1, L).

The final viton gasket holds Sn foil, and is cut in a 30x36mm rectangle (Figure 2.1, K). This rectangle has a single cut 20mm from the bottom where pieces of Sn foil can be put through. Additional details on the Sn foil contacts are listed in Chaper 2.8).

2.4 MAKING THE MIRROR ELECTRODE

A single gold mirror-electrode (ME, Figure 2.1, F) is a 1”x6mm BK7 substrate window sourced from EKSMA optics (Prod.ID#220-0203E) coated with 7nm of Cr and 200mm of Au at the Washington Nanofabrication Facility (WNF) using a sputter-coating machine. Squares of polyimide tape sourced from McMasterCarr (Prod.ID#77595A44) are cut using a CO_2 laser at the UW Makerspace facility in McCarty Hall (The Mill) to make the negative mask stickers that separates an electrode and counter-electrode region during the sputter-coating process. The PDF

files that the CO_2 cutting laser uses to create the stickers, which were created and can be edited in Adobe Illustrator, can be found on the same research filesharing platform OSF as the other CAD files. This link also features CAD files for all the parts of this SEC cell, most notably the customized parts. These stickers should be cut using the Matboard material setting on The Mill's 60W Epilog Laser Fusion M2 CO_2 laser, with a setting thickness of 0.001 inches, a vector engraving parameter set to the minimum of -50%, 11% overall laser power, a frequency value of 50 pulses/inch, and 100% raster speed. Additional instructions on how to use the laser cutter are taught by staff at the facility, and will typically be part of the necessary tool orientation required to use that tool in the Makerspace.

Once made, these stickers will be covered in a black burn residue from the cutting laser. This should be wiped off with a damp towel, ideally with an alcohol, before application. The stickers should be applied such that the center of both sides of the mirror-electrode are in the interior boundary of the sticker. The stickers can be very thin and prone to breaking – this is fine so long as the sticker is applied to the substrate with the complete shape and no gaps in broken ends that could cause metal to be sputter coated between the electrode and counter-electrode regions.

After these stickers are applied, the substrates can be taken to the WNF for Sputter-coating. The WNF has general and tool-specific training programs that will be both necessary to use those facilities, as well as the sputter coating device and the wet benches that will be relevant for creating these ME's. Specific instructions and definitions for using their Evatec LLS EVO Sputter System will be provided with this training, but the process involved doing five 3nm Cr passes and twenty-nine 7nm Au passes, all for 10 seconds with 50sccm and 2kW, except for the second presputter step. The first presputter step used 10 passes, the second presputter step used 6 passes.

2.5 FRONT WINDOW

The cell is built to accommodate a 1" (25.4mm) diameter, 2mm thick window piece (Figure 2.1, D). The window material should match the spectral application – for the IR experiments performed in this work, the windows were made of CaF_2 and sourced from ISP Optics (Prod.ID#CF-W-25-2).

2.6 PTFE SPACERS

The solution path length is defined by a polytetrafluoroethylene (PTFE) spacer (Figure 2.1, E), which can be of almost any thickness. Over the course of the various work done with this cell so far, this has been between 25μm and 100μm. These spacers are usually cut from sheets purchased from Lebow Company (Prod.ID#25TF-30x30cm, for 25μm) and cut by hand with shears to form either two ringed hemispheres or a series of small circles. It's worth noting that, since this is a reflective sample cell, the functional light path length of sample defined by these PTFE spacers is twice the actual thickness of the spacer.

2.7 SCREWS

There are a few varieties of screws used in the cell's construction (Figure 2.1, A & O). The most common are M3x0.5x10mm black-oxide steel socket head screws sourced from McMaster Carr (Prod.ID#91290A115). However, due to a small error, the screws for securing the table mount to the cell back (Chapter 2.2) are M4x0.7x10mm screws (Prod.ID#91290A144). Additionally, two more screws are used to fasten and mount two ring mounts the cell body. These ring mounts were scavenged from the UW electronics shop, as were the Phillips-head screws.

2.8 SOLDERING SN FOIL CONTACTS

Making contact with the back of the ME's electrode and counter-electrode are two pieces of Sn foil that are fed through the back of the cut in the 30x35mm gasket and folded flat to the gasket (Figure 2.1, K). Each piece of Sn foil is cut with hand shears from a sheet procured from the UW chemistry's electronics workshop to a rough 5mm by 40mm. While folded through the gasket, these Sn foil contacts should be shifted so that each piece only makes contact with either the electrode or the counter electrode, with no overlap that might cause an electrical short. After the position of the tin foil contacts are placed without shorting over the ME, they can be secured with a single piece of electrical tape on the back of the gasket, over the non-functional side of the foil contacts.

These foil contacts must also be soldered to wires, and the wires must then be soldered to the ring mounts. Soldering is best done in a fume hood to avoid inhaling the fumes from the flux in the solder, and care should be taken to avoid touching the hot components. The best way to solder the foil to a wire is to use a small weight to keep the stripped wire on top of the foil, and the foil on top of a table or thermally conductive surface. Melt the solder into a bead onto the soldering iron, then apply the melted solder to the wire, creating a secure joint. At the ring mount, tie the stripped wire around the end of the ring mount, then melt solder around the wire and mount. It's often good to solder onto a thermally conductive surface because it will rapidly cool the solder and avoid the solder melting the foil but rolling off the wire, and also helps the solder cool before adhering to anything else. Figure 2.2 is a picture of this process.

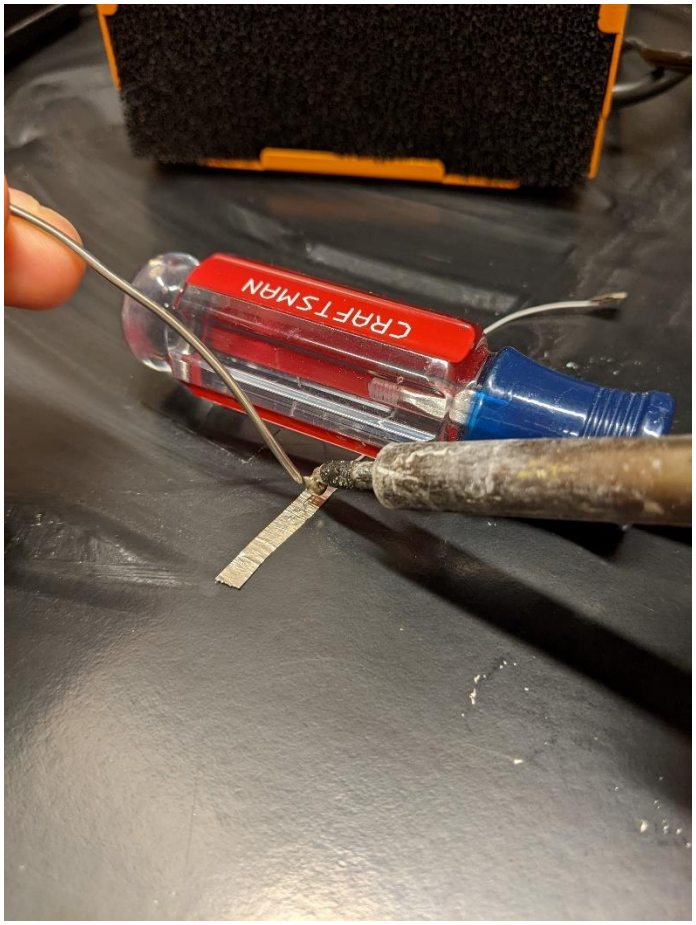

Figure 2.2. Photograph of a wire being soldered to a piece of Sn foil. The screwdriver is being used to pin down the open wire end to the Sn foil, and the solder is melted into a bead onto the soldering iron before being dabbed onto the Sn foil and the wire to create a secure connection. There is a vent fan in the background for fumes.

2.9 MODIFIED REFERENCE ELECTRODE

The reference electrode is one of the most important parts of the SEC cell. The reference electrode (RE) used in this iteration is the Leak-Free Reference Electrode, 2mm diameterx65mm length from Harvard Apparatus, inc. (Prod.ID#69-0023). This RE interfaces with the top of the ME through a port on the top of the cell. This RE was primarily chosen for its generalizable use – being leak-free, it's able to be used in a lot of different solvents (Figure 2.1, I).

To ensure a secure and fluid-tight design, the RE is interfaced with the top of the ME through a port hole leading from the top of the ME into the central body cavity of the PEEK cell body. Additionally, centered around this port, a 1/16" NPT pipe thread is bored into the top of the SEC cell body as well, and the RE is sealed into a 1/8" OD Tube to 1/16" NPT male pipe adapter (sourced from McMaster Carr, Prod.ID#5182K411) with quick-drying silicone sealant, the RE sticking out of the bottom deep enough to reach to the bottom of the SEC body port. This adapter-RE construction is then screwed into the top of the PEEK cell body for use with PTFE tape as additional sealant. Figure 2.3 is a photograph of this entire RE assembly. The RE should be stored in aqueous KCl solution when not in use to maintain its performance.

It's worth noting, however, that the RE currently used in this SEC cell is no longer sold by Harvard Apparatus, inc. The RE can be replaced by widening the port hole to fit the new RE and sealing the new RE into a male pipe-tube adapter that fits the 1/16" NPT pipe thread currently bored into the top of the cell. Any replacement RE must be at least 60mm long and no more than 5mm in diameter (6mm being the diameter of the ME).

Figure 2.3. Side (left) and end (right) photographs of the reference electrode and pipe-tube adapter assembly. The clear globule at the top is the Si sealant used to both seal the pipe-tube adapter and adhere the reference electrode to it.

2.10 Flow Tubing

Flow tubing interfaces the SEC cell from the sides (Figure 2.1, G). Two small holes are bored from the side of the cell into the central SEC cell body cavity (Figure 2.1, H), where fluid can flow. Overtop these holes are bored 1/4” NPTF pipe threaded holes, so that 1/8” Tube OD to 1/16” NPT male pipe adapters (sourced from McMaster Carr, Prod.ID#5182K411) can be screwed in with Teflon tape as additional sealant. The tube side of the adapter can then be fitted with 1/8” OD seamless 304 steel tubing (sourced from McMaster Carr, Prod.ID#89895K711). This tubing can then be bent with a metal tube bending tool into a convenient “L” shape so that the entire assembly can have a low profile but stable tubing. Additional tubing adapters and PTFE tape can be used to interface these metal tubes with rubber or plastic tubes for fluid flow.

Sometimes it's desirable to seal the cell instead of inputting flow tubing, primarily if anaerobic conditions are desired and the cell would be filled in an anaerobic glove box. This is done by simply screwing a stainless-steel plug sized 1/16 NPTF (sourced from McMaster Carr, Prod.ID#4464K559) into the pipe threaded holes that would otherwise be used for the pipe-tube adapters for tubing.

2.11 Additional Assembly Instructions

While the cell could be assembled in a variety of ways, there are many stages where issues in cell assembly can ruin the functionality of the cell, and it's worthwhile for the user to be systematic in the assembly of this SEC cell.

First, the front cover should be screwed and secured into the cell body. To ensure that there are no leaks from the front of the front cover, the front cover and the rubber gasket should be put together, and the exterior circumference of their circular components wrapped with a thin layer of PTFE tape. This PTFE taped unit can then be screwed into the cell body.

After this front cover and gasket are in place, the front window can be placed on the front gasket. The top of the front window should be approximately parallel with the fluid input/output holes on the inside of the cylindrical cell body cavity. The PTFE spacers should then be carefully placed in the proper locations, using a pair of tweezers to move them out of the way of fluid flow.

While it's still visible, a good next step would be to screw in the reference electrode adapter, wrapping PTFE tape around the threads to avoid leaks. The reference electrode adapter should be screwed in just deep enough that the reference electrode's tip is almost towards the end of its hole into the cylindrical cell body cavity.

After this, the ME can be added into the cell cavity, with the round-designed side facing the front of the cell and the top of the ME facing the reference electrode. After this, the back gasket with Sn

foil contacts can be carefully added to the back, with great care taken to ensure that the Sn foil contacts do not overlap both ME electrodes. This is a good time to use a multimeter to check for any shorts or electrical issues by testing the foil contacts for connections. If the electrodes remain separate, a multimeter reading “Overload” to the resistance measured across the electrodes or ring mounts, then it’s often good to go back and add PTFE tape to cover and seal the edges of the ME and the cell body, taking care not to cover the foil/gold contacts.

After the Sn foil contacts and rear gasket are properly set up, a soft gasket made of thermally conductive silicone rubber is put between the back of the cell and the final Viton™ rubber gasket. The thermally conductive silicone was source from McMaster Carr (Prod.ID#1272N18) and was originally chosen for an alternative setup with a thermocouple, but its primary useful property is being significantly softer than the Viton™ rubber and is much more effective for cell compression. After the final gasket is put into place, a final check with the multimeter is good before screwing the aluminum cell back into place, screwing down alternating corners to slowly ratchet the entire thing closed and compressed. After this, flow tubing can be attached as desired, or the flow tubing holes can be alternatively sealed.

Table 2.1. Bill of Materials

Vendor	Product ID#	Description/Name	Quantity
EKSMA Optics	220-0203E	1”x6mm BK7 Window	1 (or more)
McMaster Carr	91290A115	M3x0.5x10mm Black-Oxide Steel Socket Head Screw, Pack of 100	1
McMaster Carr	89895K711	1/8" OD Seamless 304 Stainless Steel Tubing, 3ft	1
McMaster Carr	1272N18	Thermally Conductive Silicone Rubber Sheet , 8" square	1
McMaster Carr	4464K559	Low-Pressure 302 Stainless Steel Plug with Hex, 1/16 NPTF	2
Lebow	25TF-30x30cm	25um Teflon Sheet	1
Harvard Apparatus, Inc.	69-0023	Leak-Free Reference Electrode, 2mm Diameter x65mm Length	1
McMaster Carr	77595A44	Polyimide Tape, 2" Squares	1
ISP Optics	CF-W-25-2	CaF2 Window: 25.4mm Diameter x 2mm Thick	1
McMaster Carr	5182K411	Yor-Lok Fitting for Stainless Steel Tubing, Straight Adapter for 1/8" Tube OD x 1/16 NPT Male	3
McMaster Carr	91251A199	Black-Oxide Alloy Steel Socket Head Screw, 8-32 Thread Size, 1" Long	1
McMaster Carr	91251A540	Black-Oxide Alloy Steel Socket Head Screw, 1/4"-20 Thread Size, 3/4" Long	1
Goodfellow	SN000232	Tin Foil, 0.03mm thickness, 300x300mm square	1
McMaster Carr	86075K24	Viton® Fluoroelastomer Rubber Sheet, Chemical-Resistant, 6" x 6", 1/8" Thick	1

Chapter 3. CELL USE AND MAINTENANCE

The following chapter is dedicated to the specifics of operating, maintaining, and troubleshooting the electrochemical components of the SEC cell. This concludes with the details and data collected from a FTIR SEC functionality test and the standard operating procedures that were informed from those functionality tests.

3.1 How to Operate the Potentiostat

Potentiostats are often very expensive, even for very simple models. This is largely because they're designed for high-precision electrochemistry, and feature complex components to ensure that precision. However, for the purposes of SEC experiments, this is unnecessary, and by building the potentiostat designed by by Dobbelaere et. al. the cost of the potentiostat was an order of magnitude lower than buying even a commercial training model with no noticeable problems and is also easy to use[26]. The potentiostat they designed also includes a Graphic User Interface (GUI) operated via a Python script and a few additional packages. The paper also includes a bill of materials, which can all be ordered from Digikey. Due to an ordering accident, two sets of parts were bought and assembled by the UW Chemistry Electronics shop staff. As such, both potentiostats have been used for experiments.

While the original paper features directions for downloading the GUI program and its required packages, this will hopefully be done already. If not, see Chapter 3.2. However, not all of this information is germane to the SEC project and running this program from the Khalil Group's wet lab only requires two steps.

First, on the desktop, locate the folder "potentiostat". Within this folder is both the original paper by Dobbelaere et. al. and a set of instructions in a text file labeled: "How to use" which can serve as a reminder for how to open the GUI. Then, open the command line with Windows+R and run the command: "python C:\Users\William\Documents\python\tdstatv3.py"

After opening the GUI, there are two primary tabs to interest for SEC experiments – the "hardware" tab and the CV tab. The other two are useful for testing batteries and other electronic devices, but not used in any SEC experiments.

In the “Hardware” tab shown in Figure 3.1, the potentiostat can be connected to the computer running the GUI with the “connect” button. The USB vendor ID (VID) and Product ID (PID) have not been changed from their default values, and will not need to change unless the microcontroller source code values are different from the ID values. The default VID is 0xa0a0 and default PID is 0x0002.

The “Calibration” box of this tab contains all the relevant options for calibrating the spectrometer, although given the electronic components this is often not necessary as the designers attest to offset or gain errors only attributing between 0.01% and 0.1% of the measured value. They recommend doing a four-step calibration process outlined part 6.3 of their work[26]. The only additional equipment they recommend for completing some of these steps is a $1k\Omega$ resistor. After calibration, pressing the “Save to Device” button saves the current calibration settings to the device’s internal memory, so these settings will automatically be reloaded from the device on GUI startup regardless of which computer it’s being run from.

The most important part of this menu for casual use, besides the connection button, is the “Manual Control” box. First, the mode can be set to “Potentiostatic” or “Galvanostatic” by pressing the labeled button. A potentiostatic setting ensures that the potential being held at the working electrode is held constant while current is measured, while a galvanostatic setting ensures that the current being passed is kept constant while potential is measured and allowed to fluctuate. While most SEC applications don’t require the current range to be limited, the “Current range” dropdown menu allows for a few options that can be applied to the device with the “set” button next to it. The last set of items in the box is a dropdown menu that selects for “Potential (V)”, “Current (mV)”, or “DAC code”. SEC applications would never make use of the “DAC code” option, but a value can be input to the text box next to the drop down menu, and by pressing the set button, the

device will set that property to that value when turned on using the “On” and “Off” buttons at the top of the box. The value can be reset while the potentiostat is on, or can be set before the potentiostat is turned on.

While using the SEC for experiments, this box is useful for setting to potentiostat mode and setting a steady potential to convert the entirety of the sample at the working electrode. The resulting current can be seen on the graph, so it’s clear to the user when, after the potential is set, a diffusion-limited current is reached. If the user wants to save the contents of the graph, they can use the “Log to file” box. By setting a file path, the GUI will continuously addend an ASCII file with the potential and current information displayed on the graph so long as the “Log” box is checked.

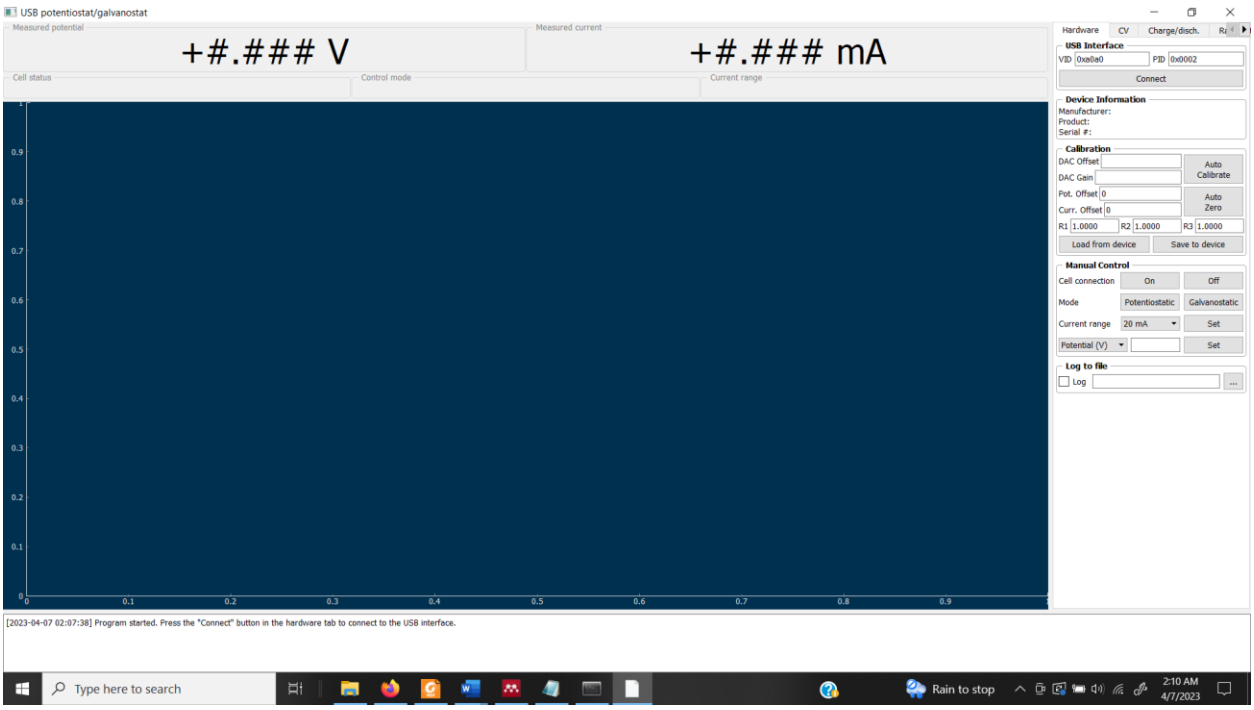

Figure 3.1. Hardware tab of the Potentiostat GUI.

The next tab worth explaining is the “CV” tab. This tab features a “Cyclic voltammetry parameters” box where the upper and lower potential bounds being cycled between can be entered, as well as the starting potential. The “OCP” button is the “Open Circuit Potential” button, which

automatically fills the Start Potential (V) entry to the currently sensed potential of the connected potentiostat. This is frequently the most efficient thing to do, although it's not of incredible importance. After this, a stop potential determines what electrical potential the cyclic voltammogram will end at after completing the number of cycles specified in the "Number of Cycles" entry. The scan rate (in mV/s) is also set here, and unless there's a specific reason the user would prefer otherwise, a good scan rate is 100mV/s. The final quantity of importance is the "Samples to Average" criteria. It's important to understand that this criteria does not affect the potentiostat's sampling rate or potential scanning speed – instead, this criteria determines how many previous samples of the potential being scanned ad the current being measured are consolidated and averaged. A larger number of samples averaged means that the cyclic voltammogram ultimately is composed of fewer sample points than the default setting of 1, where the number of samples collected and displayed is directly from the sampling rate of the potentiostat.

The "Autoranging" box features three check-able boxes that allow the user to limit the current being measured to any of those three values. While this may be useful for electronics, where current limits may want to be imposed to avoid damaging those electronics, this isn't important to SEC experiments, and all three boxes can be left checked so that any current value measurable by the potentiostat can be reached. Finally, the "Output data filename" entry should contain the full file path and file name of the ASCII file the user wishes to save. When all these entries are filled, pressing the Preview Sweep button displays on the graph the Electric Potential vs. Time graph of the planned CV, and will return an error if there's an issue with the proposed potential scanning criteria. The next two buttons will begin or stop the cyclic voltammogram sampling. Stopping the

cyclic voltammogram will save to the specified file whatever data had been collected, even if stopped prematurely.

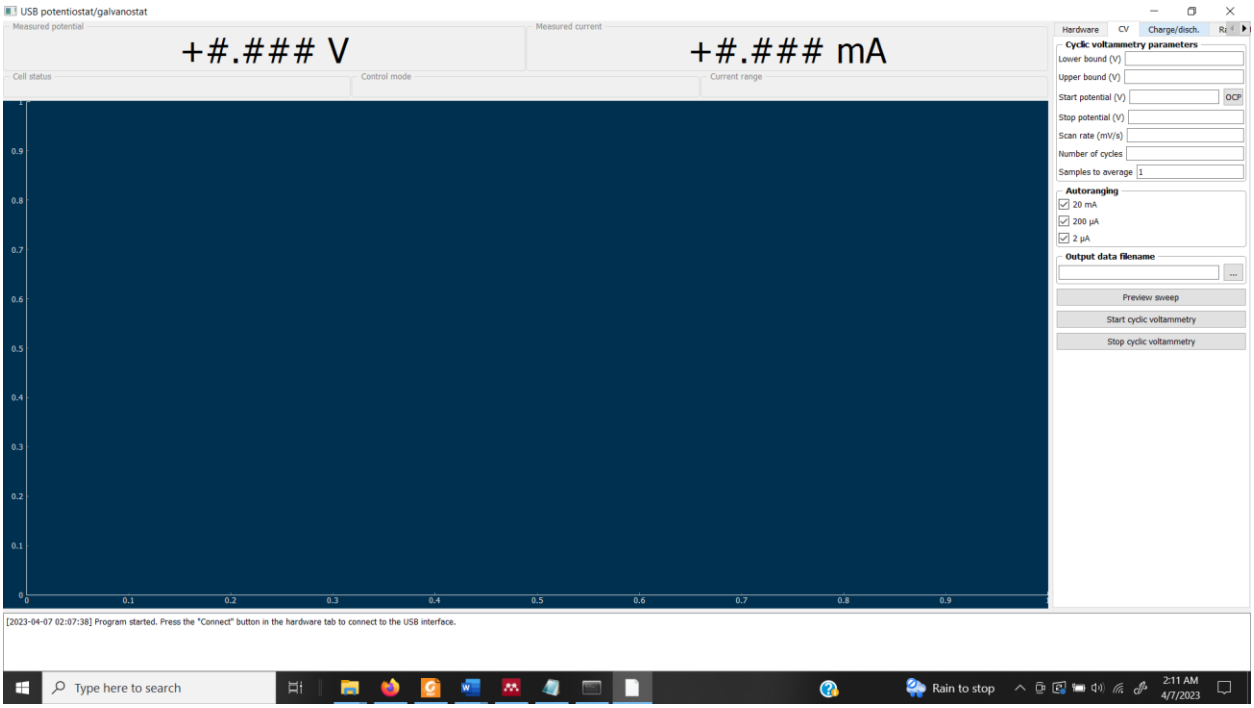

Figure 3.2. CV tab of the potentiostat GUI.

Finally, to use the potentiostat for a typical cyclic voltammogram operation, the potentiostat will need to be hooked up to the working electrode, counter electrode, and reference electrode. This is done with alligator clamps on the ends of wires screwed into contact holes in the potentiostat. To remove or replace these wires, the caps on the potentiostat simply need to be unscrewed and the wire taken out or replaced. One note important for use is that the potentiostat has four terminals, with one terminal for the WE, CE, and RE, but an additional terminal labeled as SE. This is an optional Standard Electrode, but this is not used for SEC applications. When affixing the alligator clips to the SEC cell's WE contacts, CE contacts, and RE contacts, clamp the SE clip to the same contact as the WE for all normal use.

3.2 INSTALLING THE POTENTIOSTAT GUI

For performing SEC experiments at the laser table, it's imperative to install the potentiostat's GUI program onto a laptop to operate the potentiostat within the wire range of the SEC cell. The original directions are found in the original publication, but can be summarized with additional context here. The original GUI file is written in Python 3 and can be downloaded from the same website as the other design files, and it is recommended to install Anaconda 3 to run the GUI, since Anaconda 3 also includes most of the required additional packages to run the GUI. However, the PyQtGraph package should be installed using conda by executing the command: 'conda install -c anaconda pyqtgraph' in Anaconda's command prompt. Additionally, PyUSB will need to be installed by executing the command: 'pip install pyusb' in Anaconda's command prompt. Finally, Windows operating systems specifically need to install a USB device driver in order to successfully communicate with the USB device. This is often the most involved part of the installation process. First, the libusb program needs to be downloaded from the libusb.info website or the associated github. However, to make use of this backend program, another program that generates and installs the driver specific for this computer's USB connection to the device is needed. For additional instructions, navigate to the Documentation tab on the libusb website and go to the FAQ page. From here, navigate to the "How to use libusb under Windows?" section, which features generalized instructions and a link to a wiki page. Navigating to the wiki page reveals the specific necessary instructions under "How to use libusb on Windows" and the subsection "Driver Installation". Here, it recommends using a third party program called Zadig, an Automated Driver Installer GUI application, and provides a link. Follow that link, and download the Zadig driver installer and run the application. This web page also features a link to a usage guide for comprehensive instructions. The Zadig GUI is shown in Figure 3.3.

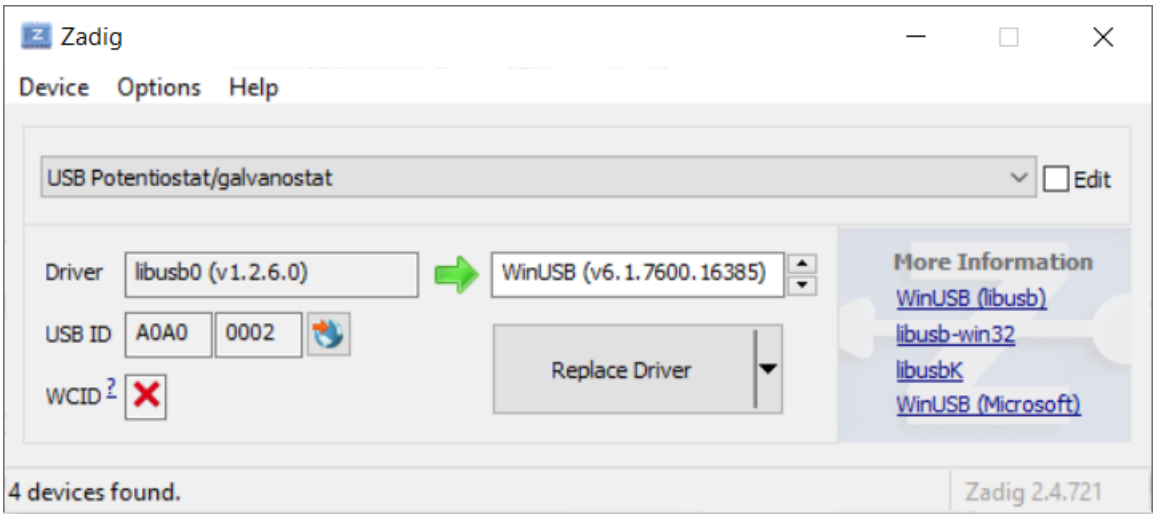

Figure 3.3. Zadig GUI, after plugging in the USB potentiostat. Since the driver is already installed, the large button reads “Replace Driver” instead of “Install Driver” as it will for a computer without an already established driver.

With the application running, plug in the USB potentiostat to the Windows laptop for installation. So long as no previous driver is installed, the USB potentiostat will either automatically populate the dropdown menu, or be one of the options available in it. Select the ‘USB Potentiostat/galvanostat’ option, and click the “Install Driver” button. Let the installation complete, and then the USB potentiostat GUI and potentiostat will be able to be used together as previously outlined.

3.3 Common Issues and Troubleshooting

The most common issue that’s found is caused when fluid leaks to the backside of the ME and comes into contact with the Sn foil. Sn is very easily oxidized, and will oxidize at potentials more positive than -0.1375V vs SHE (-0.3598V vs AgCl) so most potentials applied during the tests performed would cause the Sn to oxidize in solution. This results in uncharacterized ReDox processes occurring at the Sn foil instead of the ME, reducing overall current and altering which

faradaic processes are measured. A typical example of this is shown in blue in Figure 3.4, with a normal CV taken of the same sample after the issue was fixed in red.

Since this issue appears when the back of the SEC cell isn't sealed enough, and an in-cell CV is collected that exhibits this issue, the SEC cell will need to be drained of fluid, then disassembled and dried out. Fixing this issue always involves opening the SEC cell, and leaving remaining fluid will cause that remaining fluid to squish to the back of the SEC cell, and resume the original problem.

One potential way to fix the issue involves carefully creating a seal around the edge of the ME's perimeter with PTFE tape. It's best to do this with a pair of fine tweezers to carefully manipulate the PTFE tape to do this, and it can be difficult to create this perimeter around the ME without covering the Sn foil contacts.

Very often, the issue is best resolved by replacing the soft rear gasket with a fresh gasket. Two VITON rubber gaskets and a fresh thermally-conductive Si gasket (this material could be replaced with a different soft rubber) is enough to provide enough force on the back of the ME to stop fluid from reaching the back of the ME and the Sn foil contacts. The soft Si gasket will often permanently compress after extended use, and won't apply as much force to the contact gasket as a fresh soft Si gasket. Between replacing the soft back gasket, drying out the SEC cell interior, and carefully applying a PTFE mask, this issue will usually be resolved.

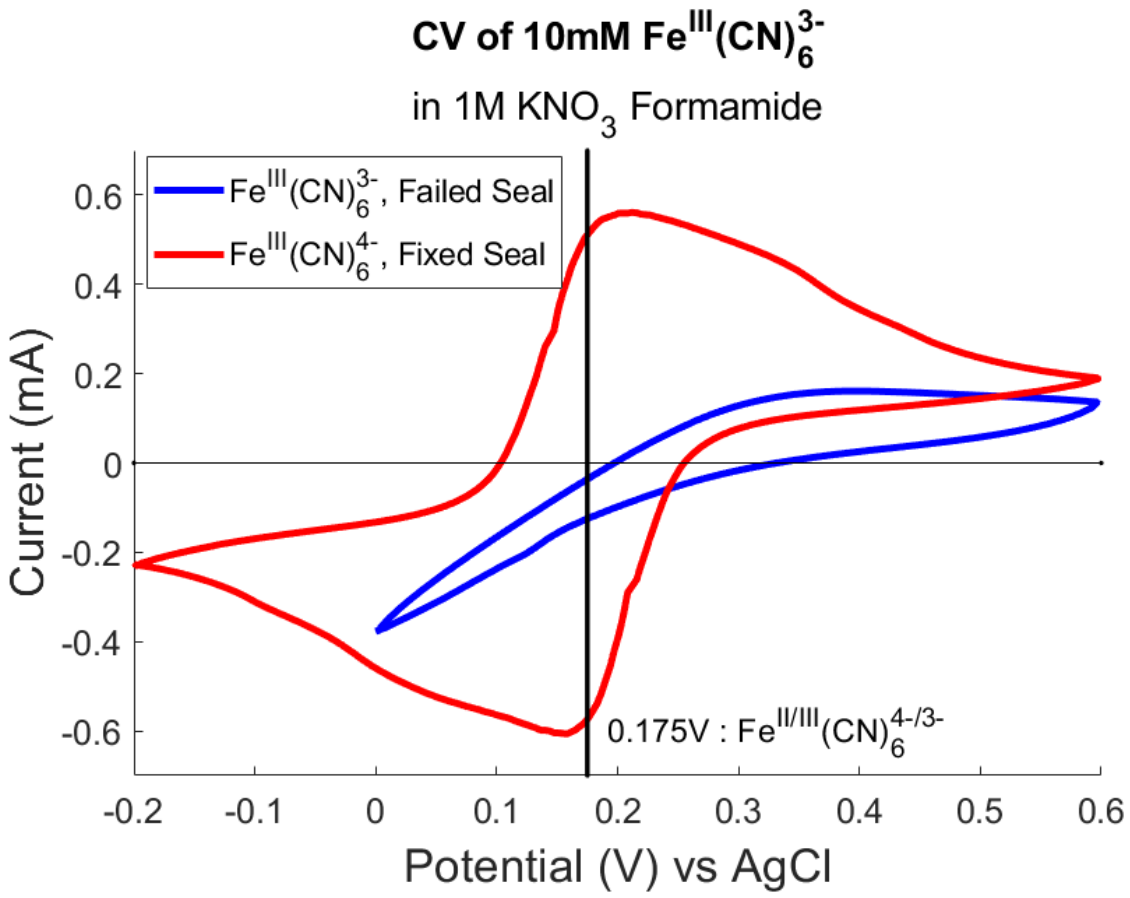

Figure 3.4. Compared, disparate quality CV's of $Fe^{III}(CN)_6^{3-}$ taken on the same day and within the SEC cell. The blue CV demonstrates the result of an inadequate seal from the back gasket, causing the Sn foil contacts to get covered in solution. The red CV demonstrates the result after all issues were fixed and the SEC cell began operating acceptably. Measured potentials are relative to an AgCl reference electrode.

A similar problem comes up when one of the components short-circuits, or passes electric current directly between the WE and CE leads of the potentiostat. When this happens, measured current becomes directly proportional to the applied voltage, resulting in a mostly flat, sloped line for a CV. Figure 3.5 demonstrates what this can look like. The slope of this line can vary widely depending on the electrical resistance the short-circuit path experiences, and thus also can be indicative of what the short might be. A short with low electrical resistance, like well-connected

wires, will have a nearly vertical slope that may result in the potentiostat hitting the current limit before it can reach its potential scan targets. What happens more often with unintentional short-circuits is that the connection isn't very sound, and thus it will feature notable resistance and the potentiostat will scan a heavily sloped CV. This can happen due to accidental contact between the foil contacts through a secondary object or the foil contacts overlapping with the WE and CE portions of the ME.

What happens more often, and can be trickier to discern, is when the short-circuit arises from a faulty ME. ME's can accidentally short-circuit its WE and CE sections during their sputter-coating, often from either a poorly applied masking sticker or if the BK7 substrate was recycled but wasn't fully stripped of its previous metal binding layer. These can lead to nearly imperceptible short-circuits, and its incredibly important to test ME's by measuring for any resistance between the WE and CE portions before using. Since the metal coatings aren't protected, it's best to do this on the back of the ME to avoid scratching the front surface. If any amount of resistance is measurable, then the ME is faulty and should be set aside as a disposable ME to be used for spectrometer alignment or to be stripped of its coatings and recycled by re-sputter coating it. It's worth noting that, after an ME has been coated in a conductive solution, it will likely display this same kind of short regardless of whether the ME is faulty or not simply because the surface becomes coated in supporting electrolyte and can pass some current, so it's difficult to determine whether an ME is faulty after it's been exposed to and electrolyte solution. ME's can be attempted to be cleaned with optical mirror wipes wetted with methanol, but this isn't recommended for ultrafast or pulsed laser applications since the unprotected ME's can be subtly scratched by this cleaning and result in beam scattering.

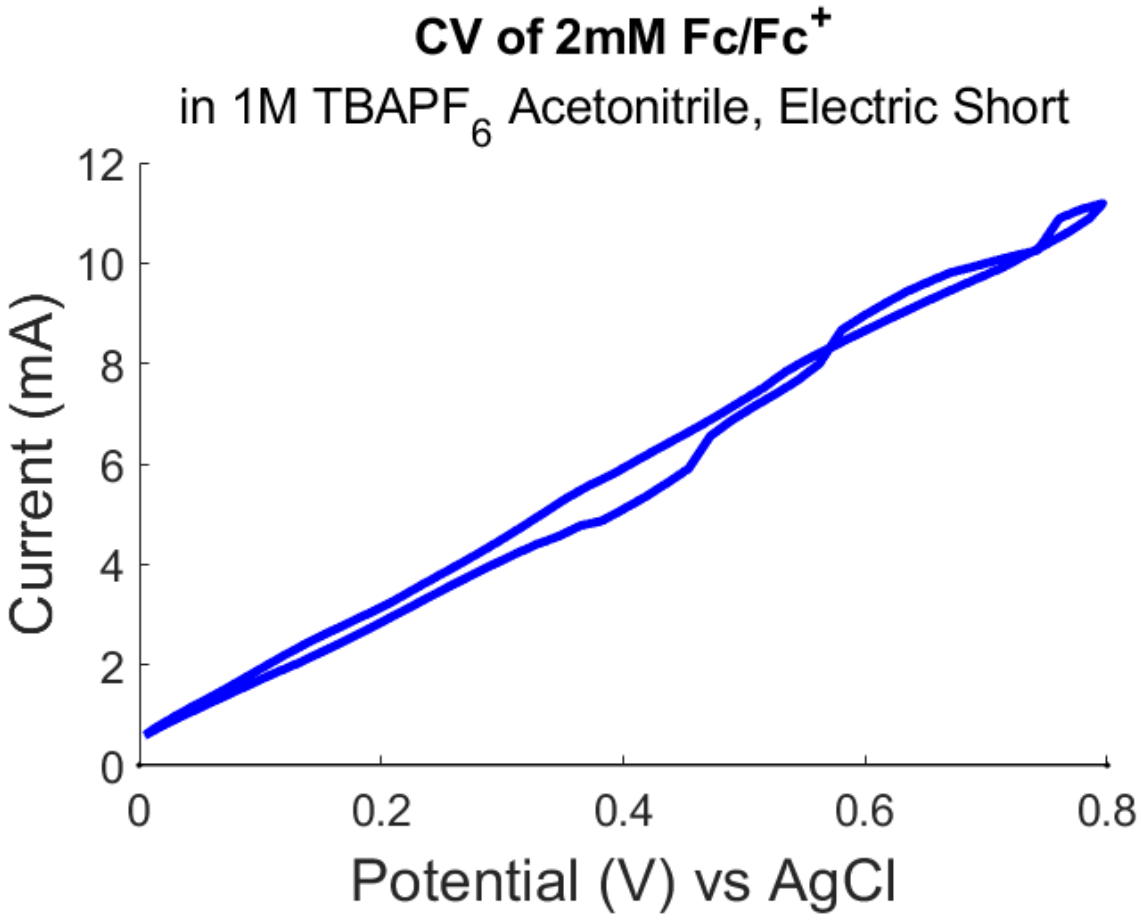

Figure 3.5. CV taken within the SEC cell when the SEC cell's electrodes were shorted. Measured potentials are referenced to AgCl.

Finally, there are times when not enough contact is made between the Sn foil and the Au ME's back side, if the back of the Au ME has significantly degraded, extremely wild but low-magnitude CV's will result where the potential cannot reach certain values, although it may occasionally jump to a very high value suddenly if the potential becomes high enough to cross a threshold, resulting in a binary current scan that doesn't reach the limits of the potential scan window. This can also manifest as generally low current, even without the strange shape. Figure 3.6 includes a couple examples of what this can look like. Solving this issue usually involves draining and opening the

SEC cell, drying out the interior, then replacing the inspecting the ME to see if its coating is flaking. If the ME coating isn't flaking, it may be worthwhile to check that the Sn foil contacts aren't overlapping the WE and CE, or make sure that any PTFE tape used to seal the edges of the ME aren't so thick that they're causing the Sn foil contacts to make weak contact

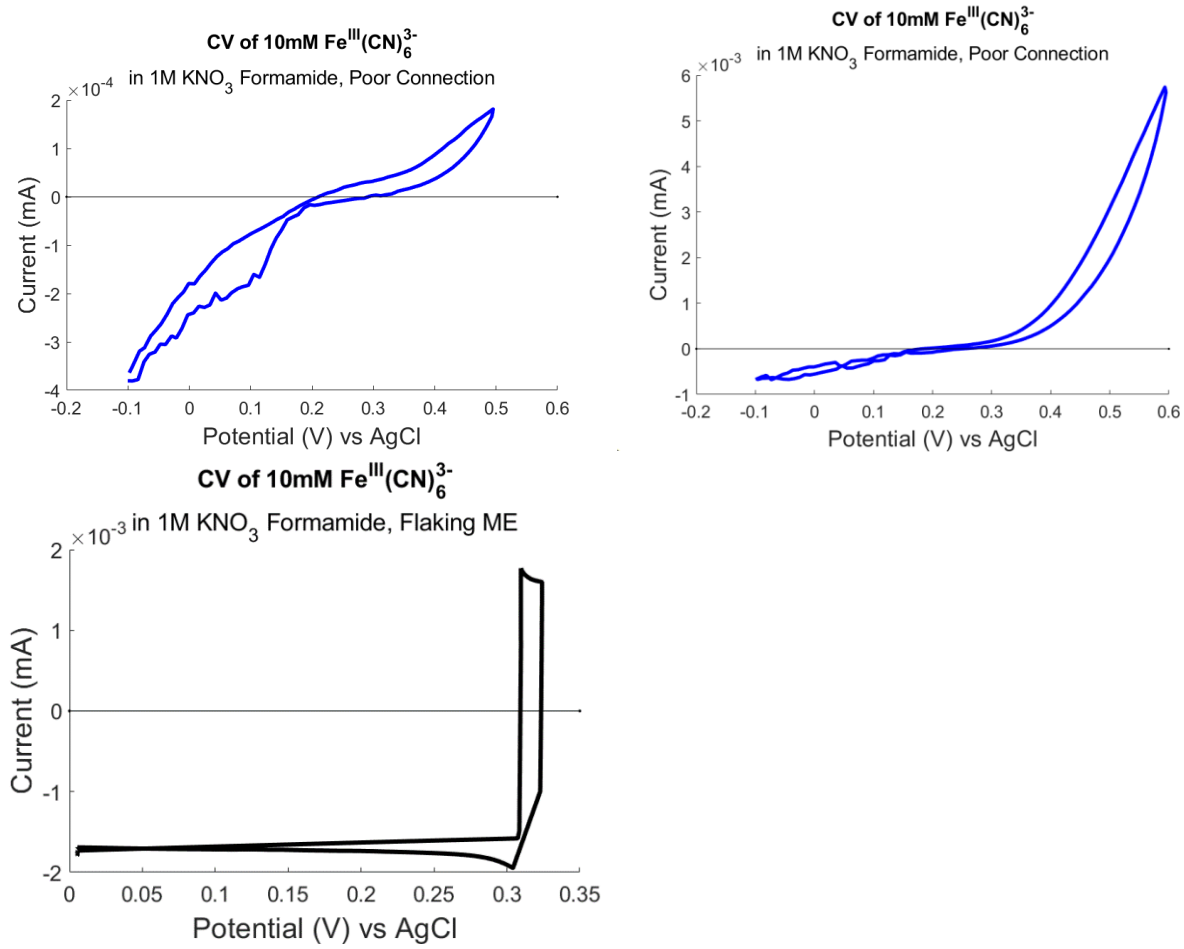

Figure 3.6. Three CV's taken within the SEC cell demonstrating various examples of poor electrical connection between the Sn foil contacts and the ME. The two blue CV's were taken when only the contact between the Sn foil and the ME were an issue. The black CV was taken, and it was revealed afterwards that this CV was the result of the back of the ME flaking off. All potentials are relative to an AgCl reference electrode.

3.4 PRACTICAL IMPLEMENTATION OF FTIR SEC

The SEC cell described in Chapter 1 was designed for use in ultrafast laser setups, where coherent beams can be focused and pointed towards the ME before being picked off, collimated, then directed towards a detector. While creating such a setup involves a modest effort on most laser tables, recreating this necessary setup is not entirely possible in a typical, transmissive Fourier-Transform Infrared (FTIR) benchtop spectrometer. Still, performing FTIR SEC experiments on a benchtop spectrometer is much easier than maintaining a customized tabletop laser system to collect a similar measurement and the massive waste of data quality and efficiency associated with using a benchtop FTIR spectrometer is outweighed by its ease and availability. To this end, I designed the SEC cell alongside an insert for the Khalil lab's Jasco FTIR 4600 spectrometer that allows the SEC cell to be used in the benchtop spectrometer and optimized to the best it can be.

3.4.1 *The FTIR Insert*

The FTIR SEC cell insert is based on a modified aluminum optical breadboard (8"x10"x1/2", i.e. 20.32cm x 25.4cm x 1.27cm), Prod.ID MB810U Thorlabs), the length of which was pared down with a metal band saw so that it would snugly fit into the FTIR spectrometer. The final breadboard dimensions are 19.7cm by 25.4cm, with no thickness adjustment. Two square mirrors are mounted to the optical breadboard in a triangular shape, and across from them is mounted a fine translation stage upon which the SEC cell can be mounted. With the SEC cell mounted and facing orthogonal to the unfettered beam trajectory, as shown in Figure 3.7, the two mirrors and the translation stage can be adjusted for an optimized transmitted intensity. This is best done using the "Monitor Sample" function of the FTIR spectrometer to quickly get feedback on which adjustments were beneficial.

As Figure 3.7 also qualitatively illustrates, the Jasco FTIR spectrometer in the Khalil lab and many spectrometers like it feature curved mirrors that focus the beam to the sample and then refocusing/collimating it with another curved mirror to the detector. Regardless of beam pointing optimization, including a reflective cell implicitly involves adding to the path length of the focused beam to the detriment of the beam focus at the detector. So far, the best average beam transmission to the detector through the empty SEC cell in this method has been 35% of the unaltered transmission. While this results in significantly lower signal-to-noise than is normally the standard for benchtop FTIR spectrometers, this is still enough transmitted light to measure FTIR SEC spectra with enough precision to discern RedOx-dependent changes in absorbance and wavelength to the sample.

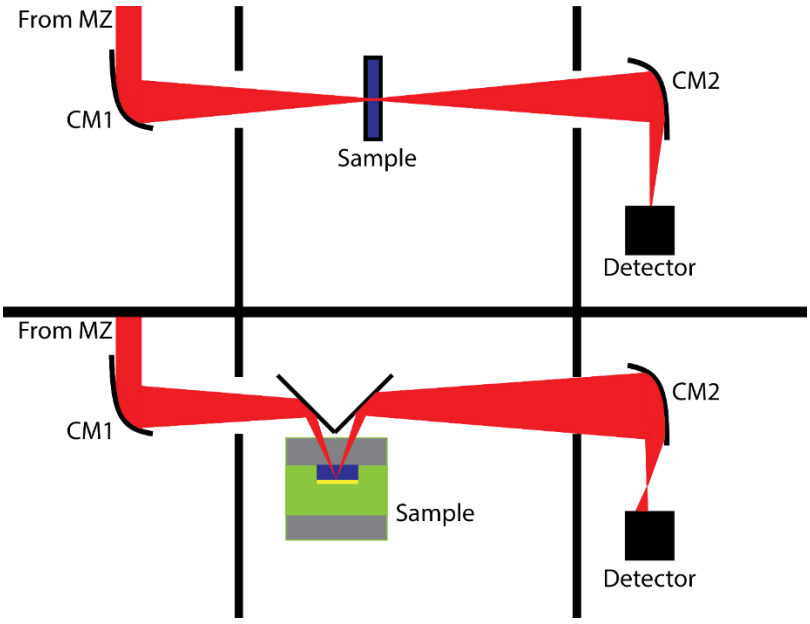

Figure 3.7. Demonstration of the FTIR insert compared to normal FTIR operation. Top: Cartoon of the normal sample area of the JASCO 4600 FTIR spectrometer. Bottom: Cartoon of the modified FTIR spectrometer interior allowing for a reflective geometry measurement. This bottom cartoon also demonstrates the issue of this design, ruining the focus at the detector due to the increased path length.

3.4.2 *FTIR SEC Data of* $Fe^{II\backslash III}(CN)_6^{4-\backslash 3-}$

Figure 3.8 **is** an FTIR SEC test on a 40nM $K_3Fe(CN)_6$ sample (Sigma Aldrich 244023) in an aqueous 0.5M KNO_3 (Sigma Aldrich 221295) solvent using the aforementioned FTIR spectrometer and SEC cell. This sample was picked for its well-reported spectra and cyclic voltammograms[27–29].

The left graph of Figure 3.8 is the SEC spectra, and demonstrates that the same spectra in the reported literature can be replicated with this SEC cell[27,28] with a signal/noise ratio of 14.476dB for the smaller $Fe^{III}(CN)_6^{3-}$ peak (calculated as $\frac{S}{N} = 10\log_{10}\left(\frac{Peak\ Max - Avg.Baseline}{Root\ Mean\ Squared\ Noise}\right)$. This spectrum was also taken within an older model of the spectrometer, a Jasco FT-IR 4100 instead of the newer 4600 model. The only difference of note is that the newer 4600 model is more successfully optimized than the previous model, with the previous model only reaching a maximum transmittance through the empty SEC cell of 25% of the unaltered beam transmission.

The right graph of Figure 3.8 shows the cyclic voltammogram taken within the SEC cell prior to taking the SEC spectra. This CV can also be referenced to previously reported CV's and demonstrates that the cell is conducting efficient, near-reversible one-electron transfer processes as expected. The measured reduction/oxidation (RedOx) potential of $Fe^{II\backslash III}(CN)_6^{4-\backslash 3-}$ is consistent with reported potentials for $K_4Fe(CN)_6$ at around 1.6mV vs the AgCl reference[29]. However, the measured peak separation for this CV is 10mV smaller than the reversible limit of 57mV. The 57mV peak splitting limit is derived with a relatively large and unchanging bulk solution. The unusually short peak separation in Figure 3.8 is to be expected because the SEC cell quickly and completely converts the small volume of analyte. For comparison, Figure 3.9

compares the CV line shapes of a standard Au disk WE and a Pt wire CE in a jar of solution, the ME suspended at the top of a jar of solution, and the internal SEC cell CV in Figure 3.9. All these CV's were conducted in the same 40mM $K_3Fe(CN)_6$ in 0.5M aqueous KNO_3 solution. This comparison shows that the current peak separation is the same for the disc and ME measuring a jar of solution, while only the ME features the thinner peak separation. This demonstrates that this sub-57mV peak separation is not intrinsic to the Au ME, but rather the interior of the SEC cell. This phenomenon is also not consistent, as inconsistencies in the SEC cell's setup and its solution (such as using a 100μm spacer instead of a 25μm spacer) can see this phenomenon disappear and the peak separation widen to a normal, 57mV reversible limit.

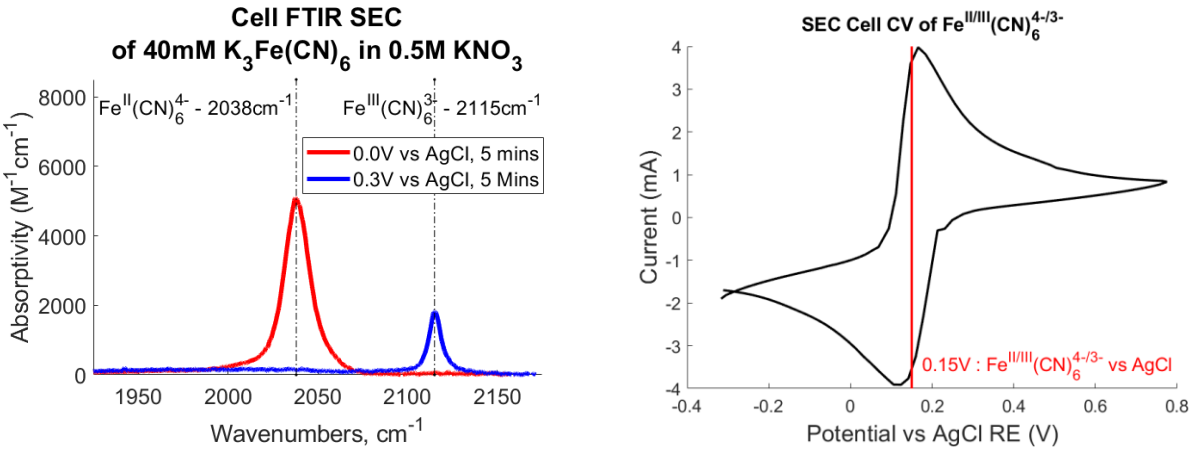

Figure 3.8. FTIR SEC of aqueous $Fe^{III}(CN)_6^{3-}$. (Left) IR-SEC spectra of 40mM $Fe^{II\backslash III}(CN)_6^{4-\backslash 3-}$ in aqueous 0.5M KNO_3 solution. The red spectrum was taken with the potentiostat holding 0.0V vs AgCl and refers to the reduced ($Fe^{II}(CN)_6^{4-}$) species while the blue spectra was held at 0.3V vs AgCl and refers to the oxidized ($Fe^{III}(CN)_6^{3-}$) species. (Right) Cyclic voltammogram of 40 mM $Fe^{II\backslash III}(CN)_6^{4-\backslash 3-}$ in aqeous 0.5M KNO_3 solution with a 100mV/s potential scan rate performed within the described SEC cell. Potentials are referenced to a AgCl electrode.

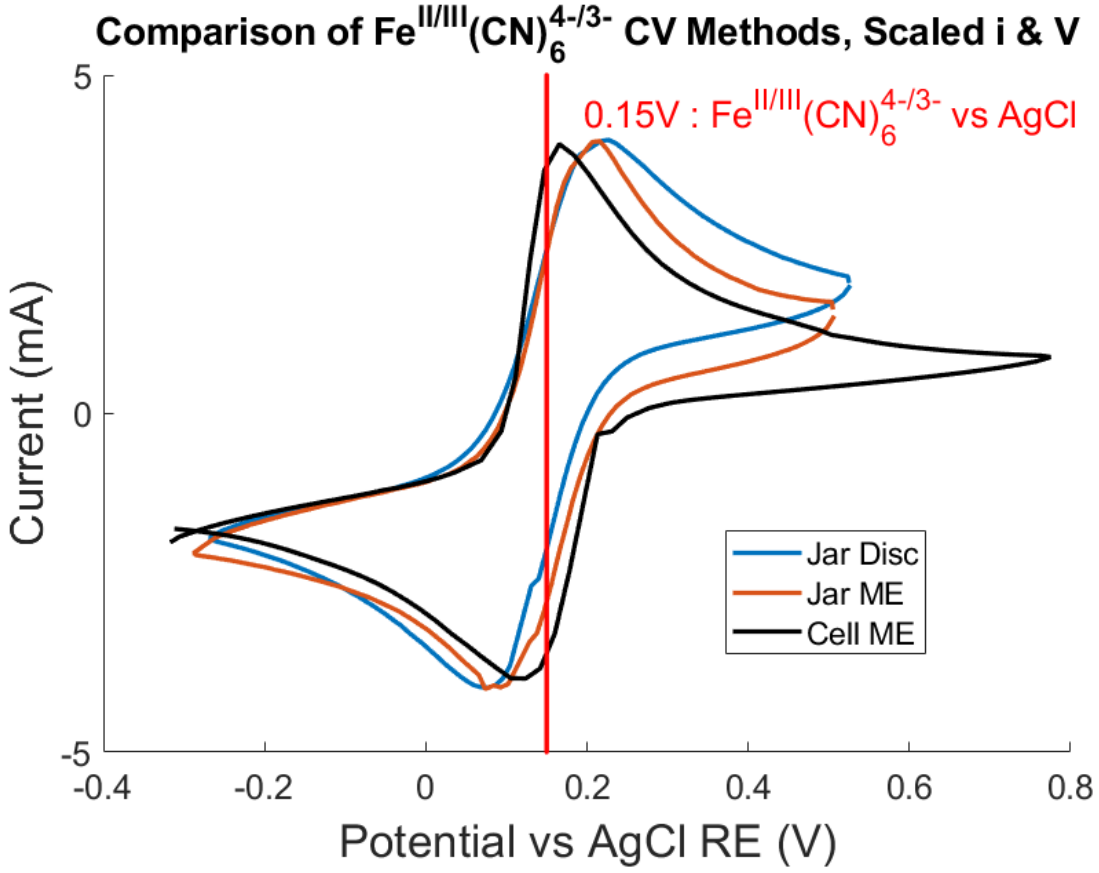

Figure 3.9. Comparison of three CV's taken with different methods. The blue CV was measured with a commercially bought Au disk WE (Biologic) and a Pt wire CE in a jar of 40mM $K_3Fe(CN)_6$ in 0.5M aqueous KNO_3 solution. The red CV was measured by suspending the front face of a ME on the surface of that same jar of solution. The black line was the CV taken within the SEC cell with a 25µm spacer and the same solution. The current values of the disc electrode and the jar ME were scaled such that their peak height matched the SEC ME current peaks in order to better compare the current peak separation.

Ultrafast SEC experiments can often take long periods of time, and it is important that any SEC cell optimized for ultrafast experiments is characterized for long-term use to inform appropriate standard operating procedures are developed that ensure the analyte is measured in the desired oxidation state. Figure 3.10 and Figure 3.11 demonstrate two different problematic approaches. Figure 3.10 represents the IR-SEC measurements of $K_3Fe(CN)_6$ taken at varying times after the

applied 0.0V potential was turned off. After the potential is turned off, $K_3Fe(CN)_6$ diffuses from bulk solution in the flow tubing onto the WE and the reduced $K_4Fe(CN)_6$ diffuses away from the WE, resulting in the loss of reduced species absorption and appearance of oxidized species absorption in the IR-SEC spectrum. If it's prudent to turn the SEC cell potential off during measurement of stable analytes, the cell also needs be filled and sealed without flow tubing to avoid this diffusion after the analyte OS is completely converted.

Figure 3.11 demonstrates an opposing approach – holding the applied potential within the SEC cell for long periods of time. This approach is useful for some analytes with desired yet unstable oxidation states. The figure demonstrates, however, that if the SEC cell is held at a potential for increasingly long periods of time, the WE become less effective at maintaining the desired oxidation state population as ions form thicker, stationary layers on the WE that impede access for analyte diffusing towards it. Additionally, this surface layer may create undesirable conditions that enable undesirable side-reactions, leading to unusual, asymmetric and shifted absorbance signals seen in the IR SEC spectrum[30]. If holding a potential for long periods of time is required for the IR SEC experiment, it is advisable to include the SEC cell's flow tubing and/or limit time the analyte remains in one oxidation state before switching the applied potential. Switching the applied potential after at least 180 minutes minimizes erroneous signal, and even after 1200 minutes a combination of changing the potential and flowing fresh analyte solution was sufficient to return function to the SEC cell and recreate the IR SEC signals demonstrated in Figure 3.8.

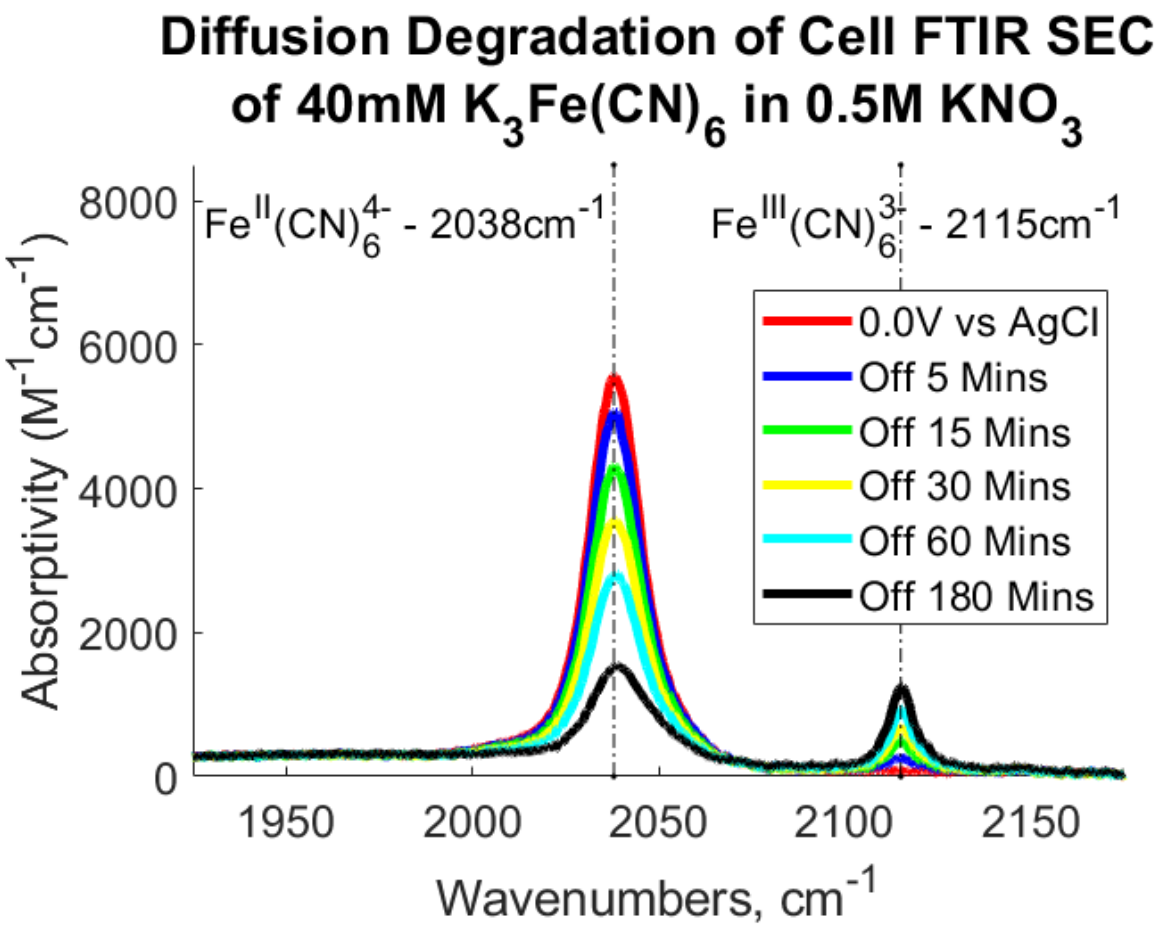

Figure 3.10. Time series of FTIR spectra of 50mM $K_3Fe(CN)_6$ in 0.5M KNO_3 initially at 0.0V, then taken again 5, 15, 30, 60, and 180 minutes after the device was shut off.

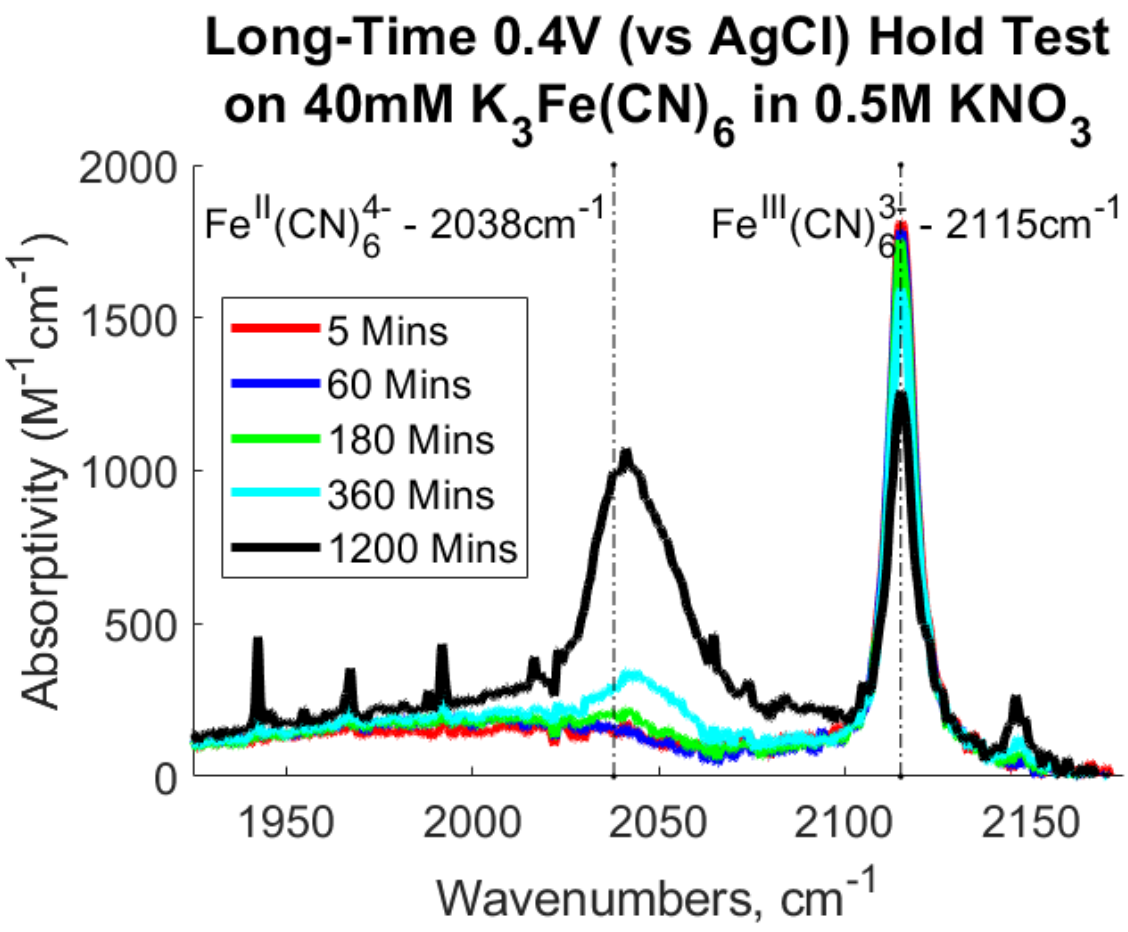

Figure 3.11. FTIR spectra of 50mM $K_3Fe(CN)_6$ in 0.5M KNO_3 held at 0.3V for a 5, 60, 180, 360, and 1200 minutes. The lost oxidized product results in an asymmetric peak centered at 2040 cm^{-1} (symmetric peak at 2038cm^{-1} is $Fe^{II}(CN)_6{}^{4-}$) .

Chapter 4. PPIR AND 2DIR LASER EXPERIMENT AND VI DETAILS

This chapter outlines major laser table details and practical necessities for running PPIR and 2DIR experiments that were used in this work. This includes a detailed description of the newly developed Labview programs required to use this PPIR and 2DIR infrastructure.

4.1 LASER TABLE INFRASTRUCTURE

The laser infrastructure was not the primary focus on this work, and much of the foundations of this system were set up and used in previous experiments. Still, in order to bring PPIR and 2DIR capabilities back into this lab, new infrastructure was built over the course of this work. This section briefly mentions what parts pre-existing laser infrastructure were germane to this work, briefly outlines which parts were added over this work, and focuses primarily on the standard operating procedures for setting up PPIR and 2DIR experiments.

4.1.1 *MIR Laser Table Diagram*

I implemented a 2DIR laser setup derived from the pre-existing 2D VE setup and shown in Figure 4.1. A 1kHz regenerative amplifier provides pulses that are routed through an optical parametric amplifier (OPA) coupled with a difference frequency generation (DFG) setup to generate mid-IR (MIR) pulses ideally centered around 2000 cm^{-1}. The MIR pulses are overlapped with a visible HeNe (633nm) continuous wave laser to aid with alignment. Before the colinear beams travel through the interferometer, they pass through a double-wedge that reflects ~10% of the incoming MIR pulse to generate a lower power MIR probe and a MIR reference. This wedge can be easily removed and reset to switch between 2DIR and 2DVE setups. The transmitted beam (here on referred to as the pump beam) is passed through a wheel chopper that's calibrated to block every other pump beam pulse. The pump beam then travels through an interferometer splits the beam and temporally offsets those pulses by a variable delay, τ_1, before collinearly recombining them to form the MIR pump beams. The MIR probe is sent through another translating stage to be offset from the MIR pump pulses by a variable delay τ_2. Furthermore, the HeNe colinear with the pump beams is also interfered and its interference pattern is used as a real-time benchmark to accurately

measure τ_1 throughout an experiment. One of the MIR pumps and the probe are then focused using an off-axis parabolic mirror into the reflective sample cell. For the works presented here, the reference beam line was not used because the additional alignment constraints were ultimately too taxing given the current spectrometer and detector setup, but they're included in the Figure 4.1 and Figure 4.2. The other MIR pump beam is directed to a single-channel mercury-cadmium-telluride (SCMCT, Infrared Systems) detector where its MIR pulse interference can be measured.

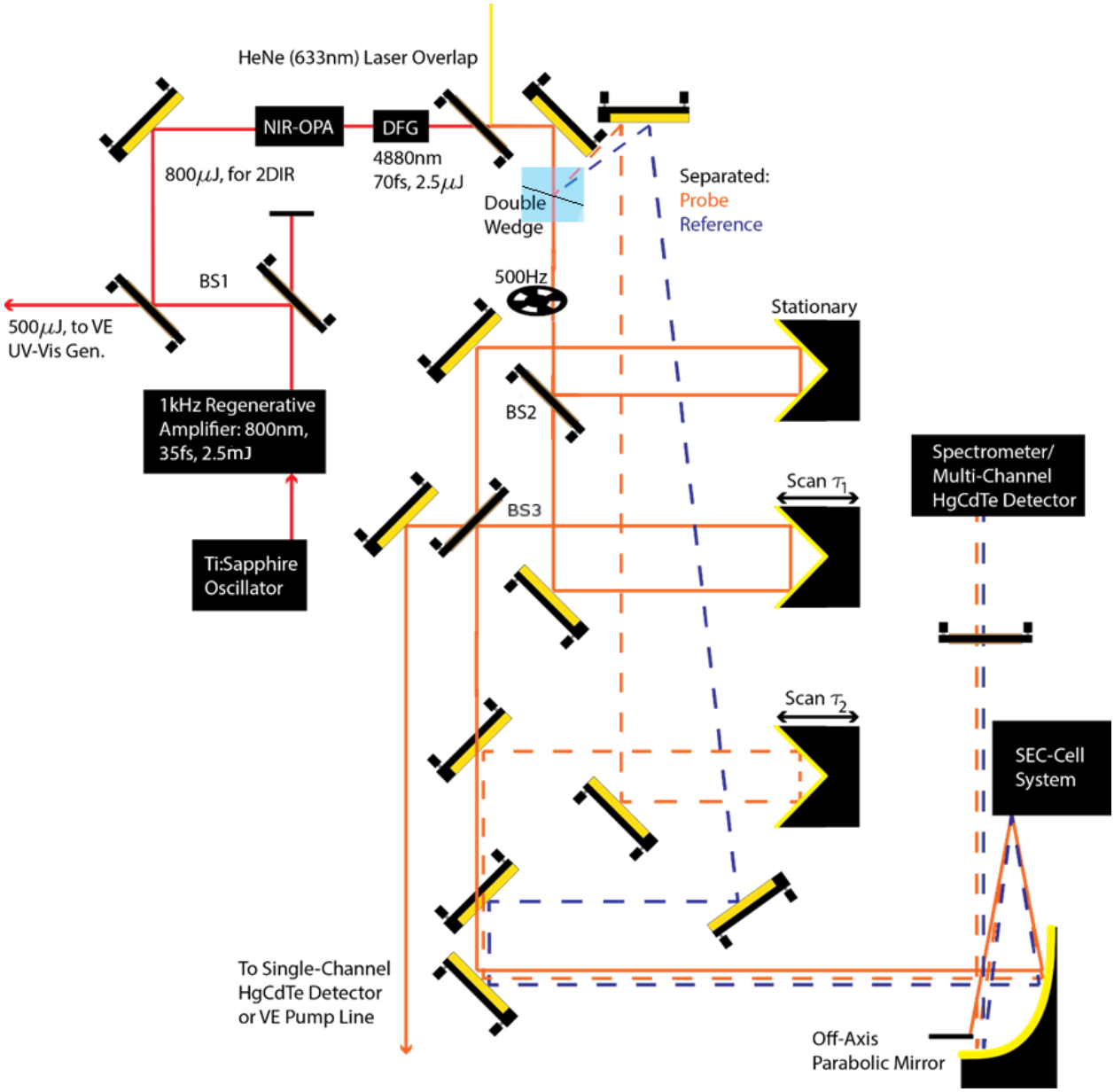

Figure 4.1. Diagram of the germane laser table setup. BS1 and BS2 refer to the two sets of two beamsplitters. BS1 attenuates output laser power and splits the beam for IR and Vis-NIR generation, while the other splits and recombines the beams in the interferometer. The wheel chopper chops at half the laser repetition rate (500Hz)

After the pump and probe beams are reflected off their focal point on the surface of the ME, the beams reflect back onto the off-axis parabolic mirror. Conveniently, this reflection should reflect

the beams approximately to the point on the off-axis parabolic mirror that should collimate them. After being reflected back off the off-axis parabolic mirror, the pump beam is blocked and the probe beam (and reference beam, if applicable) are reflected and aligned into the same beam path used to direct the transmissive probe to the spectrometer.

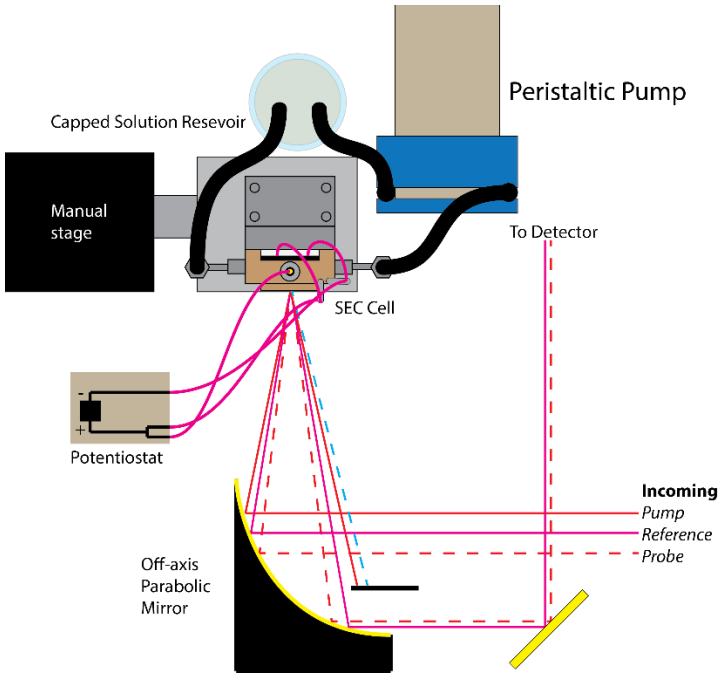

Figure 4.2. Diagram displaying beam geometry and experimental infrastructure surrounding the 2DIR SEC cell.

The spectrometer is a Horiba model iHR320 with three different blazed gratings. The grating used for the following work was 50 grooves per mm/6000nm blaze/24923. The grating and spectrometer disperse the beam across a 64x2 pixel mercury-cadmium-telluride (MCT) array, or the multi-channel MCT (MCMCT), which measures and detects all signals using the Infrared Systems FPAS2 data acquisition system and processed using a customized version of their Labview software.

4.1.2 *Fast Scanning*

In addition to the HeNe laser overlapped with the MIR beams for the sake of alignment, another HeNe beam is aligned vertically parallel to the MIR beams along with additional infrastructure for the purposes of performing fast scanning and characterizing the MIR pump spectra. This fast scanning setup has been previously described for our research group [31] and this same infrastructure is used for collecting and processing 2DIR spectra in this work. However, instead of collecting the required HeNe and MIR interferograms using a separate data acquisition board as per the 2DVE experiments, these are collected by the Infrared Systems FPAS2 data acquisition system and processed with a customized version of their Labview software.

4.1.3 *Aligning a Reflective Geometry*

I had to plan protocols which our research group optimized for aligning a reflective cell on a laser table otherwise designed for transmissive spectroscopy. Aligning a reflective geometry can be more time consuming because down-table alignment and the position of the reflective sample cell are intrinsically tied, yet the cell position must be adjusted to optimize higher-order spectral signals.

The first step of the unique process for aligning the reflective MIR geometry is to first find and optimize PPIR signal in a germanium wafer with a transmissive geometry and to note the PPIR τ_2 timing between the pump pulse (in this setup, with no τ_1 separation between pump pulses generated in the interferometer) for future use as the established $\tau_2 = 0$. Ge has a reasonably strong PPIR difference signal reported in the literature and shown in Figure 4.3**.** This step would be done immediately after aligning all previous parts of the laser table, ensuring that both pump and probe beams are roughly parallel out of the interferometer, and aligning and optimizing MIR probe transmission through a 150μm pinhole via changing the pinhole's z-axis position along the probe

beam and then aligning the MIR probe to the optimized focus of the probe. The transmissive Ge difference signal will be measured using the zeroth-order probe signal through the Horiba spectrometer and multi-channel MCT.

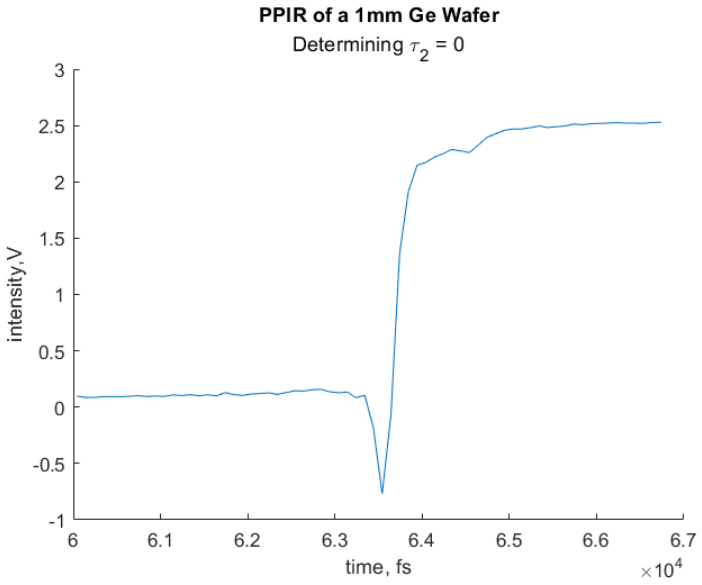

Figure 4.3. Measured PPIR difference signal of a 1mm Ge wafer as a function of scanned τ_2. Signal plotted is left as raw detected MCMCT signal in V of the 0th-order signal, τ_2 is reported as stage time in femptoseconds (fs) relative to the middle position of the τ_2 translation stage.

After a transmissive PPIR signal is optimized in Ge and $\tau_2 = 0$ timing is found and confirmed with existing literature[32], the SEC cell should be assembled in a unique and temporary method. The SEC cell should be assembled without flow tubing or connected to the potentiostat, but using defunct, undesired, or previously used ME instead of a fresh ME or the ME that is desired for use in the future experiment. Additionally, a 1mm Ge wafer should be assembled into the SEC cell between the front PTFE spacers and the ME, in the region where the sample would normally be found. The PTFE spacers should remain and function to keep the Ge wafer from scratching the front window. This entire assembly, with its table mount, should be mounted onto the same translation stage used to adjust the position of the Ge wafer used to find transmissive signal. The

SEC cell's front face should be perpendicular to axis between the two off-axis parabolic mirrors, so that the surface is flat with respect to all incoming beams and that reflected beams are reflected to the correct portion of the off-axis parabolic mirror to be collimated. Additionally, the SEC cell's Ge wafer needs to be put approximately at the focus on the MIR beams.

Once the SEC cell is mounted to the correct angle and roughly positioned to focus the incoming beams to the Ge wafer, the outgoing beam must be aligned via one posted mirror and one flip-able mirror (not shown in Figure 4.2) to introduce the reflective probe beam into roughly the same alignment as the transmissive probe beam alignment using the transmissive probe alignment irises. This should bring the MIR probe to the spectrometer for measurement. After this, the MIR probe timing stage should be set to the $\tau_2 = 0$ point and the z-direction position of the SEC cell should be scanned to locate a reflective PPIR difference signal from the Ge wafer. As the z-direction position is adjusted, the two adjustment mirrors and the transmissive alignment irises should be used to compensate for the beam's deviation as the SEC cell's reflection changes the MIR probe beam alignment. Once the reflective PPIR difference signal for Ge is found and optimized for the SEC cell's position using the translation stage, note down the X, Y, and Z direction translation stage settings for future use and block the pump beam. Optimize the reflective probe alignment after the SEC cell using the two aligning mirrors where possible, transmissive alignment mirrors where necessary (also not shown in Figure 4.2), and optimize the position of the focusing lens (omitted from Figure 4.1) into the spectrometer to mitigate any collimation issues remaining from the off-axis parabolic mirror reflection. These alignments should be done by optimizing the zeroth-order beam transmission through the spectrometer.

Once this is done, the SEC cell can be removed while the SEC's table mount should be left secured. This way, the SEC cell can be removed and returned to its properly set location with minimal

adjustment required afterwards – adjustments only being required within the mechanical tolerance of the removable plate that the table mount is fastened to on the translation stage. At this point, the SEC cell can be disassembled and fully re-assembled with the proper ME and no Ge wafer, attached to flow tubing and/or filled with fluid, and at this point it's optimal to test the electrical functionality of the cell by conducting an in-cell CV on the sample solution before replacing the SEC cell into the laser table mount. Once the SEC cell's electrical performance is verified with a satisfactory CV, the SEC cell can be replaced onto the laser table mount, any alignment fixes can be made as necessary, and the SEC cell's z-direction position can be adjusted with $\tau_2 = 0$ in order to find the PPIR signal of the analyte sample. Given the 1mm depth of the Ge wafer, this adjustment should not require more than +/-2mm of adjustment. It may also be desirable to use the SEC cell's potentiostat to hold a potential if a specific RedOx species has an easier PPIR difference signal to identify. Once the PPIR signal has been found in the analyte, final mirror alignment adjustments post-SEC cell can be made to compensate the probe beam shifting from the translation stage adjustments, and the PPIR experiment setup is complete.

4.2 ULTRAFAST FPAS2 VI AND ASSOCIATED VI'S

Almost all the laser table infrastructure used for 2DVE and 2DIR experiments is controlled with Labview virtual instruments (VI's), and I had to develop new VI's for PPIR and 2DIR applications. Some additional VI's were more quickly developed for the purposes of trouble-shooting issues with the FPAS2 data acquisition system, and these VI's are all described here for instructional direction.

The PPIR, TIR, and 2DIR functionality are both part of a single VI, labeled FPAS2_Ultrafast_2DIR.vi and found in the FPAS2_Ultrafast_2DIR Folder V15 folder in the 2DVE lab's computer. This VI is an extensive modification and update to the Infrared Systems VI

that was shipped with the FPAS2 data acquisition system, and serves as an objective upgrade to that VI by losing no capabilities but gaining others.

4.2.1 *FPAS2_Ultrafast_2DIR.vi, Basic Functions*

Figure 4.4 shows the first tab of the FPAS2_Ultrafast_2DIR_V2 VI. While most features and information are dependent on which tab is selected in the "Scan Data Type" drop down selection, a few features at the top of the menu are universally used. The "Setup" button under System Configuration to the top left opens a separate menu where the Gain and Trim values of each input channel to the FPAS2 data acquisition system. The first 64 of the 80 available channels are dedicated to the 64 pixels of the MCMCT detector's pixels, while the remaining 16 channels are external channels. Channel 14 is typically where the chopper channel is plugged into, is the only external channel required for PPIR experiments. For 2DIR experiments, the SCMCT should be plugged into external channel 2 and the two photodiodes that detect the HeNe interference for fast scanning are plugged into channels 5 and 6. Within this menu, the GAIN and TRIM settings of the SCMCT channel should be set to 0, because the SCMCT's output voltage is very high compared to the input criteria of the external channels, and the transmitted signal needs to be shrunk as much as possible in order to avoid being electronically flattened from hitting the maximum value.

Next on this menu are the integration settings, both displayed and adjustable with the "Integration Setup" button. Pressing the button will bring up a menu where the integration time and integration delay can be adjusted universally for all channels. These are usually adjusted for the detected laser pulse, but it might be feasible in the future to adjust this integration time to improve signal acquisition from external channels, since the integration from external channels can't be adjusted separately. The tests demonstrated here were done using 1994ns of integration time with a 50ns delay.

The input for “Number of Scans” for determines the number of scans to be averaged for each spectrum to be taken on the current tab. This is true for all tabs except for the 2DIR tab. The “Total Number of Channels” input is left at 80 unless an FPAS2 data acquisition device with more external channels is used or a new detector.

The “Chop Sync Channel” input is always set to the external channel that the chopper synchronizing signal is plugged into, which again is usually channel 14. The Chopper Threshold input setting is set to 2.5V, which is the post-gain signal of the chopper synchronizing signal being detected by the FPAS2 detector.

The “Read” button loads the file specified in the file path input line below onto the graph for all non-transient scan tabs. The “Save” button saves the current graph contents to a file specified by the file path written below.

The FPAS COM Port drop down menu specifies which port the computer port that the FPAS2 is plugged into. Usually, that’s COM1.

These function as the primary controls for the Background Scan (B), Chopped Mode (open – blocked), and Sample Scan (S-B) (ref-sig) tabs. Additional controls are exclusively on the Time-Resolved Scan (S-B) and 2DIR tabs.

For the Background Scan, Chopped Mode, and Sample Scan tabs, as all shown in Figure 26, each tab features three graphs. The fist graph is the averaged spectrum detected from the 64 pixels of the MCMCT detector with raw intensity measured in volts. The second graph tracks the detected signal intensity over time, measured in milliseconds (which coincides with the number of scans per averaged spectra) per pixel, each pixel being a different colored line. The third graph of those three tabs depicts the measured standard deviation, in volts, for each pixel over the course of the collected scans in the averaged spectra.

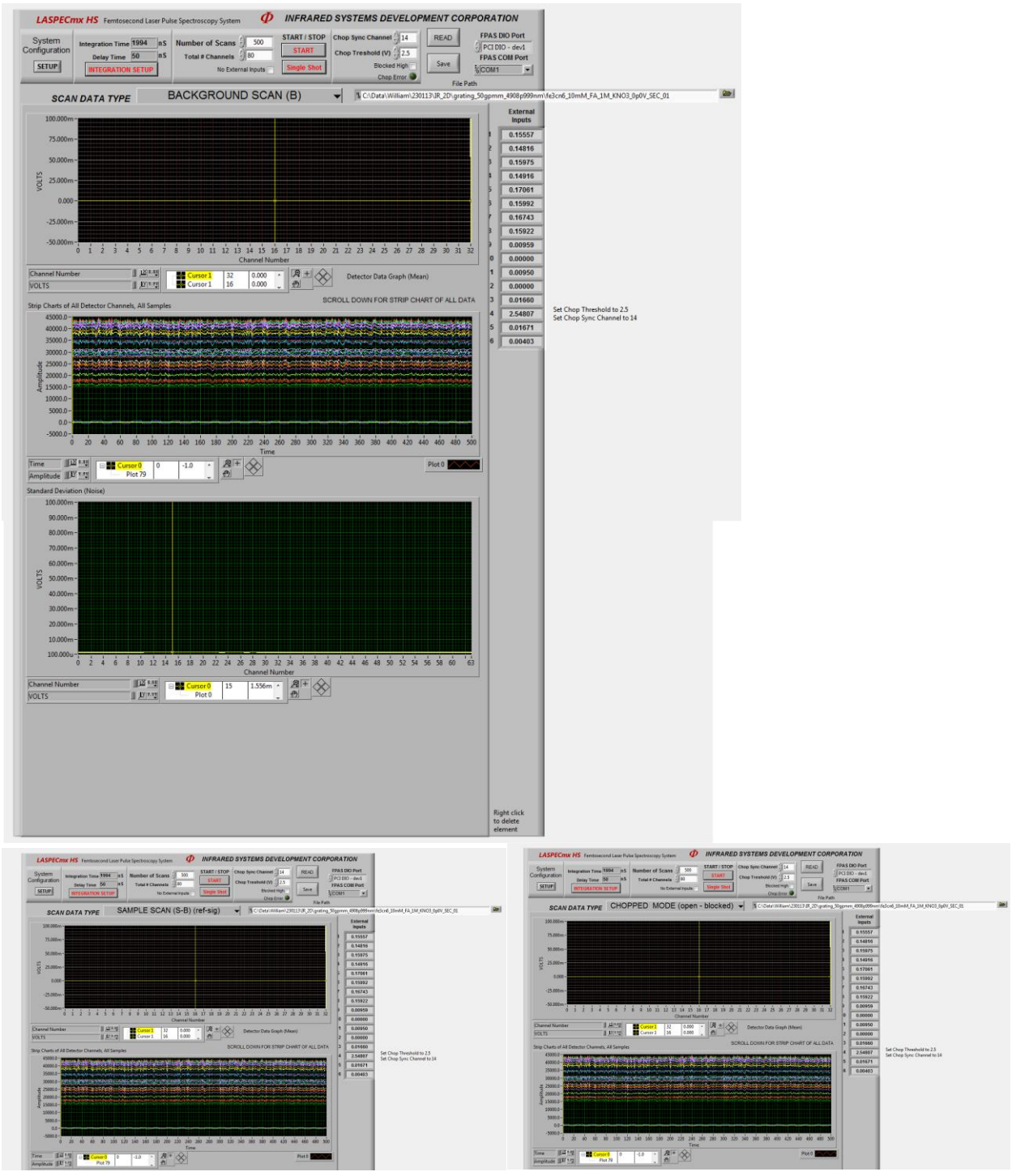

Figure 4.4. Background (top), Sample (bottom left), and Chopped (bottom right) tabs of the FPAS2_Ultrafast_2DIR.vi GUI. The bottom two pictures have non-unique lower components cut off for brevity.

4.2.2 *FPAS2_Ultrafast_2DIR.vi, Time-Resolved Scans*

The next unique tab of this VI is the Time-Resolved Scan tab, which is shown in Figure 4.5**.** While the top of the page remains consistent, the tab features many unique inputs and displays unique graphs. The first item is the table which contains Start, Stop, and Step Size entries that are entered per row of the table. Each row of the table represents a unique scan range which will move the remote translation stage specified as "Stage Name" from the stage position respective to the time entered in the "Start Time" to the stage position for the "Stop Time" in increments derived from the "Step Size" input. At each interval, the FPAS2 will collect and average the number of shots specified in the "Number of Scans" input and average them to measure the signal at that τ_2 time delay. A sub-VI converts the times input in femto-seconds into a stage position in mm. This stage position is then displayed in the "Current Stage Position" indicator, which is just below the "Current Row" indicator that displays which row of the table is currently being scanned through. At the end of each row of data collected, the VI saves the time-dependent averaged signal per pixel, the time-dependent standard deviation per pixel, and an array of the time delays that were measured.

The first graph of this tab displays the most recently collected averaged signal spectrum, per pixel. The second graph displays the most recently collected spectrum's standard deviation per pixel. The third graph updates to display all the time-delay dependent signals measured so far within the current row of time delays for any pixel numbers entered into the "Display Channels" table just above the graph. Pixels that the user wishes to display must be put into the Display Channels table before the experiment for the VI to graph the time-dependent signal for those pixels.

Finally, pressing the Stop button ends the current data collection run after finishing the current scan.

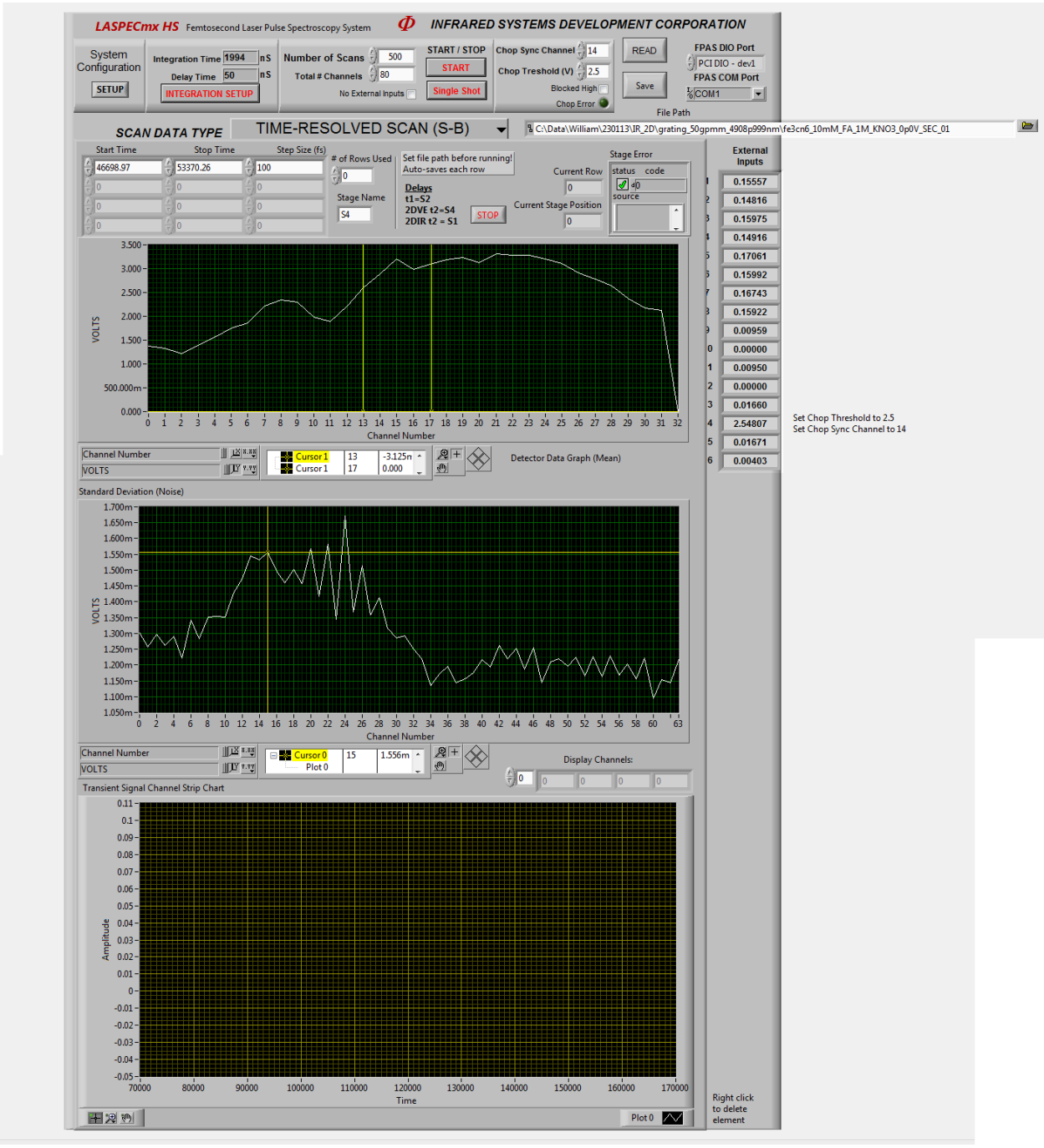

Figure 4.5. Time-Resolved Scan tab of the FPAS2_Ultrafast_2DIR.vi GUI.

4.2.3 *FPAS2_Ultrafast_2DIR.vi, 2DIR*

The final tab of note within this VI is the 2DIR tab, which is shown in Figure 4.6. Performing a 2DIR experiment first requires performing a PPIR experiment, the instructions Part A of this chapter. After setting up and performing a PPIR experiment, the τ_1 stage can be scanned in order to collect a 2DIR spectrum. This is done asynchronously using the XPS network GUI on the lab computer, where the τ_1 stage should be scanned about 150fs before $\tau_1 = 0$ and about 1800fs after $\tau_1 = 0$ at a rate of 0.03mm/s using the Cycling function of the XPS Front Panel GUI. While a τ_1-scanned FTIR using the SCMCT would have been collected earlier, it's good to collect another using the beam line not being used for the pump beam. Once the fast scanning is well-aligned up to the SCMCT with the unused MIR pump beam line, the SCMCT output should then be plugged into channel 2 of the FPAS2 external inputs, and the two photodiodes should be plugged into channels 5 and 6 of the FPAS2 external inputs, respectively.

Once all the 2DIR infrastructure is set, the 2DIR VI's inputs can be filled out. The unique inputs to the 2DIR VI begin with setting the "Samples per τ_1 Scan, which is the number of shots measured for one τ_1 scan that can be displayed on the first graph and individually saved. Noting the laser's pulse frequency of 1kHz, 1000 scans represent one second of τ_1 scanning and data collection. The next input is the "# of τ_1 Scans per τ_2", which determines how many of the previously allotted τ_1 scan sampling periods will be collected before advancing to a different τ_2 stage position. Each τ_1 scan is individually saved, then all τ_1 scans taken for the current τ_2 stage position are loaded, averaged, and plotted as a 2DIR graph on the first graph. This helps to quickly troubleshoot potential issues with the 2DIR graph, decide if data collection should be pre-emptively ended, and to see if increased averaging is continuing to improve data. If 2D plots aren't desired, perhaps to save time spent processing between τ_1 scans, the "Plot 2D?" button can be deselected.

The input for "τ_2 Stage Name" controls which stage is moved for τ_2 timing. This is usually the MIR probe line's remote translation stage (input as S1), but could feasibly be re-assigned to another remote translation stage if desired.

The next set of inputs are "Photodiode 1 Ch.", "Photodiode 2 Ch.", and "SCMCT Channel", which should all be set to the external channels where each is respectively plugged into the FPAS2 data acquisition device. As established previously, these should be 5, 6, and 2 respectively. Each of these channels is selected because of their properties. The photodiode channels can be plugged into any of the functioning integrated, negatively polarized external channels (EXT5-8). The SCMCT, however, should be plugged into the positively polarized, integrated channels (1-4).

The next set of inputs are the τ_2 rows, which function almost identically as their previous iteration on the Time-Resolved Scan tab. The last novel part of the 2DIR VI is a set of unique indicators. First, an error output indicator relays XPS error messages and other error messages directly to the GUI for troubleshooting. The Current τ_2 position, listed in femptoseconds, as well as the current τ_1 scan of that τ_2 position, are displayed by their respective indicators. Finally, three Boolean indicators labeled "Uneven Shots", "τ_1 stage bool" (a name probably worth changing), and "Binning Error". "Uneven Shots" indicates a shot chopping error, "τ_1 stage bool" lights up if the τ_1 scanning stage isn't moving, and "Binning Error" indicates an error in the HeNe fast tracking that assigns bin values to each shot.

The second graph plots all relevant data collected from the fast-scanning process concurrently collected from the previously mentioned external inputs. These data include the MIR pump pulse interferogram collected over the previous T1 scan in Volts/shot (ms), the bin number assigned to each shot of the previous scan, and the signal read from each photodiode. While the graph's legend

suggests that the chopper signal is also plotted, this is largely vestigial as the data plotted on this graph are filtered from shots that are detected as having the pump beams chopped.

The third graph on this tab plots the processed HeNe interferogram data collected at the two photodiodes for the previous T1 scan. This previously described data processing method[31] should ideally plot the resulting data as a circle, the regularity and continuity of this circle indicating whether the HeNe interferogram data could be reliably used to sort data into appropriate temporal bins.

Before running this VI, the user should use the FPAS2_FastScanTest_V2, which is in its namesake folder within the lab VI folder.

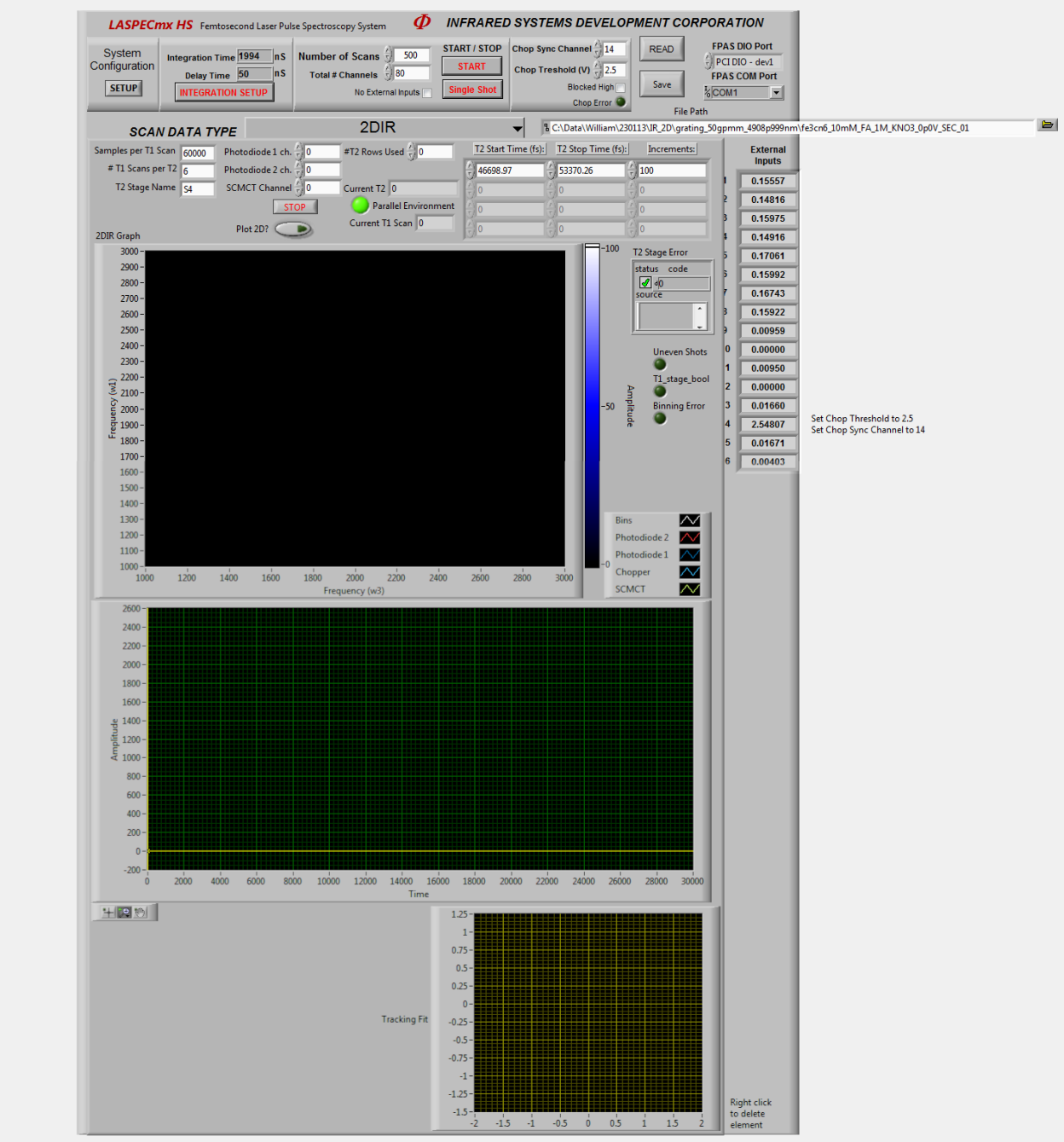

Figure 4.6. The 2DIR tab of the FPAS2_Ultrafast_2DIR.vi GUI.

4.2.4 *FPAS2_FastScanTest_V2.vi, Chopper Test*

Figure 4.7and Figure 4.8 show the unique tabs of interest in the FPAS2_FastScanTest_V2 VI, which all serve the purpose of setting up and/or troubleshooting connections into the external channels of the FPAS2.

The first of these tabs, specifically shown in Figure 4.7, is the Chopper Test tab. This is a default tab that's normally included into the base FPAS2 VI and is operated with the default controls and settings described before. Despite the images shown in Figure 4.7, this tab displays very different graphs. Notably, it displays nothing on the first and third graphs, and instead primarily uses the second graph to plot the detected signal from the chopper's electronic synchronization per shot, which is plotted alongside a static plot depicting the value alternating between 0 and the Chop Threshold value for each shot, which would be ideal. The other major focus of this VI is the Chop Error Boolean indicator in the upper menu, which lights up whenever the chopper signal alternation isn't aligned with the ideal plot. This VI depicts how frequently or under what circumstances chopper errors occur, which can be useful for troubleshooting issues with the pulse chopper. If, for example, the chopper signal isn't alternating at all, it's possible the wrong pulse chopper is connected to the FPAS2 or active.

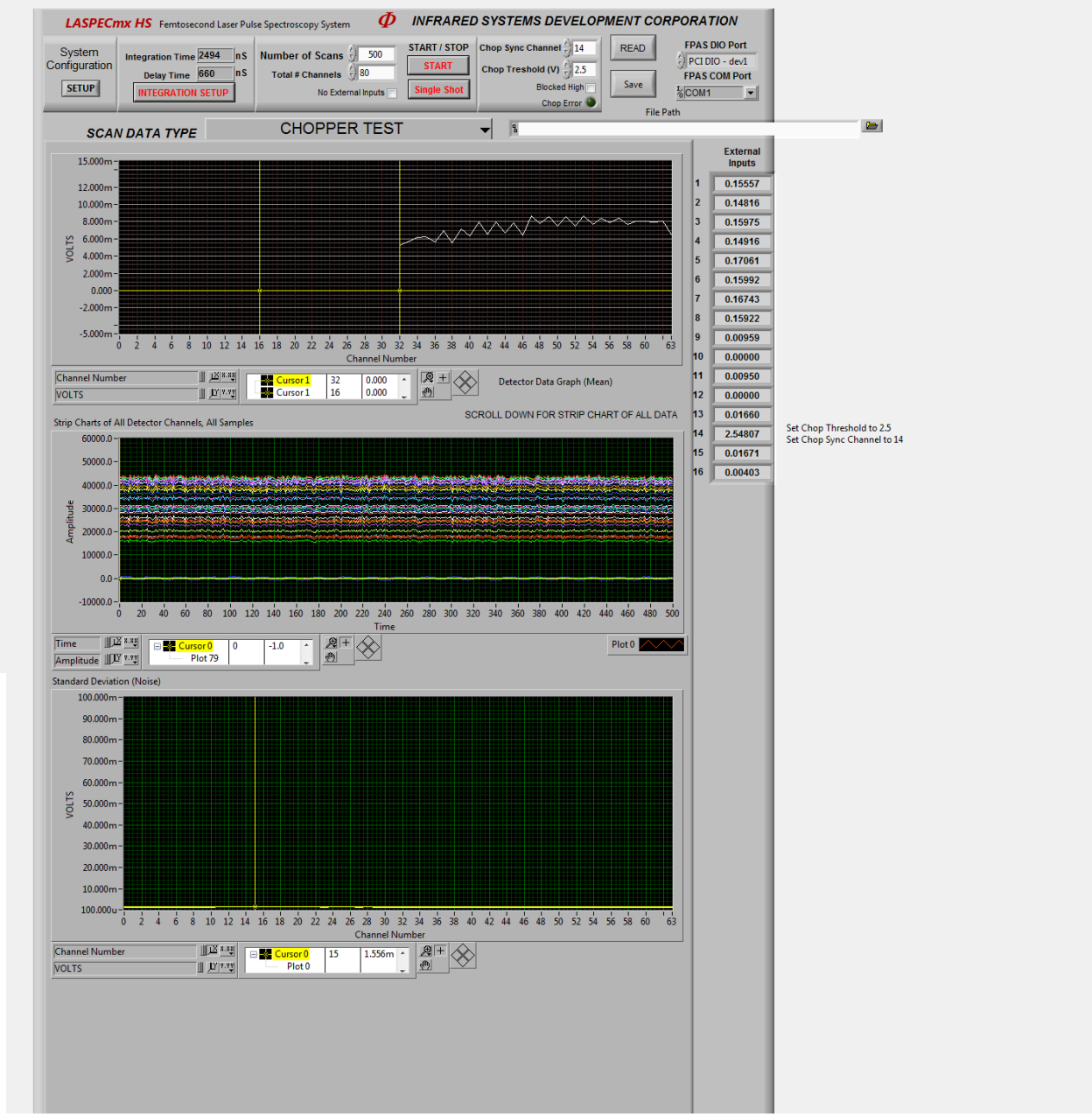

Figure 4.7. Chopper Test tab of the FPAS2_FastScanTest_V2.vi GUI.

4.2.5 *FPAS2_FastScanTest_V2.vi, External Input Plotting and Fast-Scanning*

Figure 4.8 shows the Display External Input and FastScan Test tabs of the FPAS2_FastScanTest_V2 VI. These were developed quickly out of necessity, so they're cumbersome to use and the VI the Display External Inputs tab's function will frequently require

the entire VI to be forced to stop running and restarted in order to change the settings. The Display External Input tab requires the user to select an external channel using the "index (row)" input. With this input filled and the Start button pressed, the VI will collect a number of samples using the FPAS2 specified in the Number of Scans input and continuously update the plot with the most recent data set. This is extremely useful for directly measuring and plotting the signals being plugged into the external channels. This process is essential for ensuring that MIR pump pulse interferograms collected at the SCMCT during 2DIR measurements are collected properly, since even with the Gain and Trim of the SCMCT channel being set to a minimum value, the signal from the SCMCT measuring the MIR pump interferogram will usually saturate the FPAS2's detection limits and filters will be needed to significantly reduce the electronic signal measured and transmitted by the SCMCT. A better method, in the future, would probably to maintain the greater measured signal at the SCMCT but to electronically scale down the signal before it reaches the FPAS2's integrated channel. This kind of functionality can also be used to troubleshoot issues with the HeNe fast-scanning photodiode external inputs as well.

The second tab displayed in Figure 4.8 is the FastScan Test tab. This tab has five unique inputs: "# of τ_1 Scans", "Samples per τ_1 Scan", "Photodiode 1 Ch.", "Photodiode 2 Ch.", and "SCMCT Channel". The photodiode channels should be plugged into channels 5 and 6, and can be specified as such here. The SCMCT channel should be plugged into channel 2, and also specified here. These are all the same inputs found in the 2DIR tab of the FPAS2AcqMain_Ultrafast_2DIR VI, however this tab in this VI does not collect any data from the MCMCT. Instead, it collects all data required for fast scanning using the FPAS2 data acquisition device. This tab, unlike the 2DIR VI, also does not filter collected shots based on whether they're chopped and fast scanning data via this tab should be collected with the chopper turned off. However, like the 2DIR tab of the

FPAS2AcqMain_Ultrafast_2DIR VI, it plots the circular fit of its HeNe interferogram data and SCMCT-collected MIR pump pulse interferogram, albeit more prominently in this VI. This tab also features the same Boolean troubleshooting indicators and τ_1 scan indicator that the 2DIR VI features. Despite many of these functions being redundant with the 2DIR VI, it's often useful to measure these data separately before performing 2DIR experiments, particularly in this separate VI that's dedicated to FPAS2 troubleshooting. This VI tab is especially useful for confirming the overall viability of the HeNe photodiode and SCMCT inputs being collected by the FPAS2 that can be superficially optimized or troubleshot in the Display External Input tab. Unlike the Display External Input tab, data collected through this tab is saved to the file path specified in the universal controls.

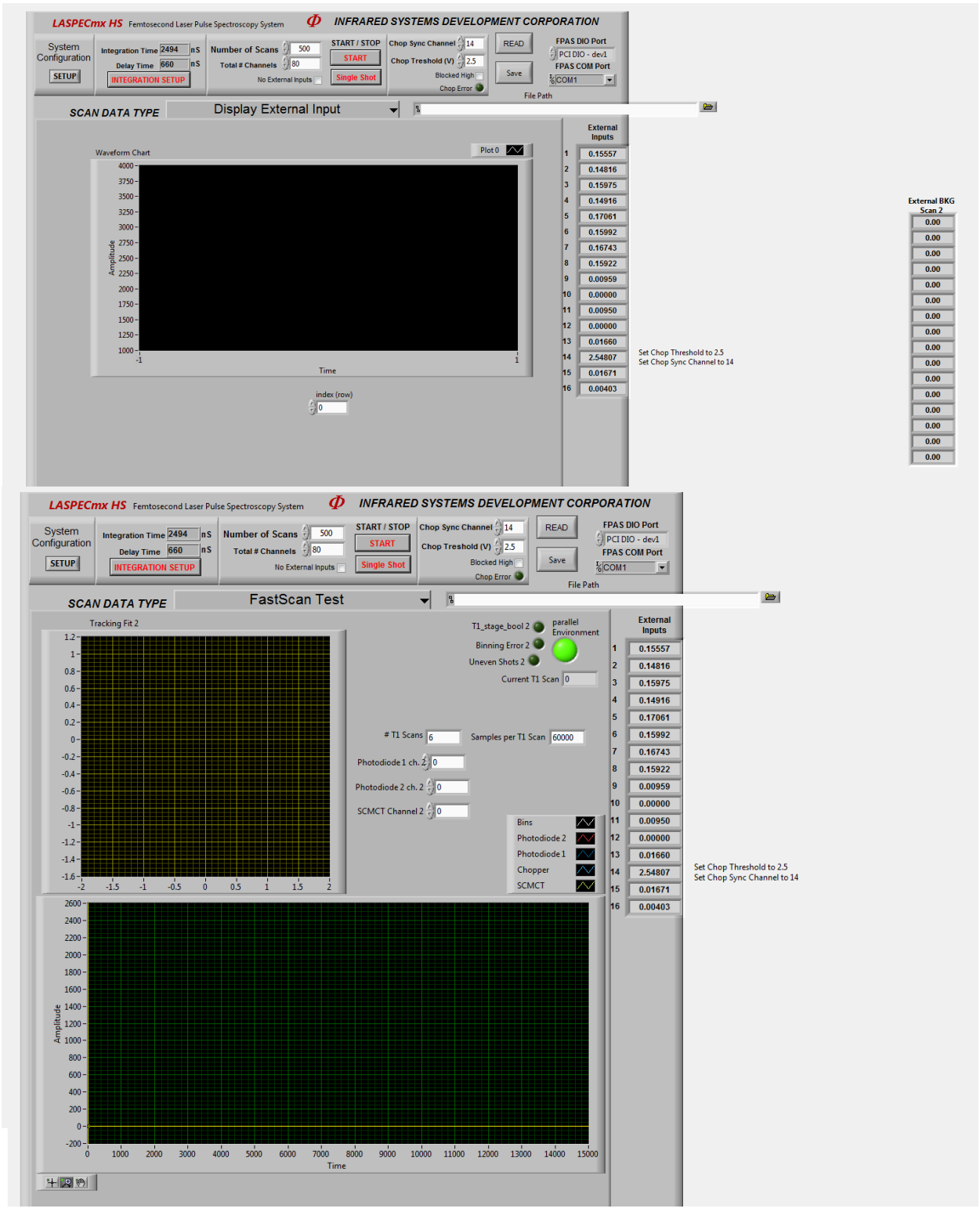

Figure 4.8. Display External Input (top) and FastScan Test (bottom) tabs of the FPAS2_FastScanTest_V2.vi GUI.

As a final note, it's worth re-iterating here some unique idiosyncrasies regarding the external channels of the FPAS2 data acquisition device. Channels 1-12 all integrate their signal using the same integration parameters as the MCMCT detector, effectively making those integration parameters universal for all channels. Channels 13-16 are not integrated, and instead the signal positively-polarized signal is read out at the end of the 1kHz acquisition period without any integration period or set delay. All channels except channels 5-8 read exclusively positively polarized voltage, which can be an issue if a device either uses negatively polarized signal or switches between positive or negative polarized voltages, as no inputs to the FPAS2 can accept both polarizations. This is potentially an issue for the HeNe-detecting photodiodes, which are capable of outputting both positive and negative voltage and can cause very slight discrepancies in assigning temporal bins.

Chapter 5. DEMONSTRATING ULTRAFAST SEC FUNCTIONALITY VIA $Fe^{III}(CN)_6^{3-}$ PPIR

This chapter begins with a brief tutorial on how to understand and interpret PPIR spectra, then overviews the PPIR SEC experiment as part of the culmination of this work.

5.1 PPIR PRIMER

PPIR is an ultrafast spectroscopy technique performed by pumping the analyte molecule from its vibrational ground state to its first excited vibrational state with a powerful IR laser pulse before being measured after a time delay via a weaker probe pulse, which will measure the red shift in the analyte's absorption spectrum from being in the excited state as a function of that time delay, usually referred to as τ_2. This red-shifted absorption spectrum is derived from the fact that various

inter and intramolecular forces make IR active vibrational modes varying degrees of anharmonic, and is effectively measured by plotting the difference between the unpumped, ground state vibrational spectrum and the pump-excited vibrational spectrum. This difference spectrum will always have a net negative "bleach" feature at the ground state absorption derived from both depopulation of the ground state synonymous with the population of the excited state as well as stimulated emission of the excited state by the probe pulse. The PPIR difference spectrum will also invariably feature a red-shifted, positive excited state absorption depicting the extremity and magnitude of the shifted peak. In these experiments, measuring the decay of this difference spectrum as a function of the τ_2 delay time informs the investigator of the lifetime of the vibrationally excited state. The excited state lifetime of the vibration is representative of the inter and intramolecular energy transfer mechanisms associated with that vibration. This phenomenon for a single, hypothetical molecular vibration is depicted in Figure 5.1, and $Fe^{II}(CN)_6^{4-}$) is conveniently well represented by this depiction and the spectral results of the depicted pulse and ladder diagram can be seen in the PPIR spectrum of $Fe^{II}(CN)_6^{4-}$ in Figure 5.1. Both the measured anharmonic spectrum shift and the vibrationally excited state lifetime can then be used to great effect when performing comparative experiments with additional experimental degrees of freedom, such as developing intuition for how a molecule is solvated or kinetic models for how vibrational energy is transferred throughout a molecule[33].

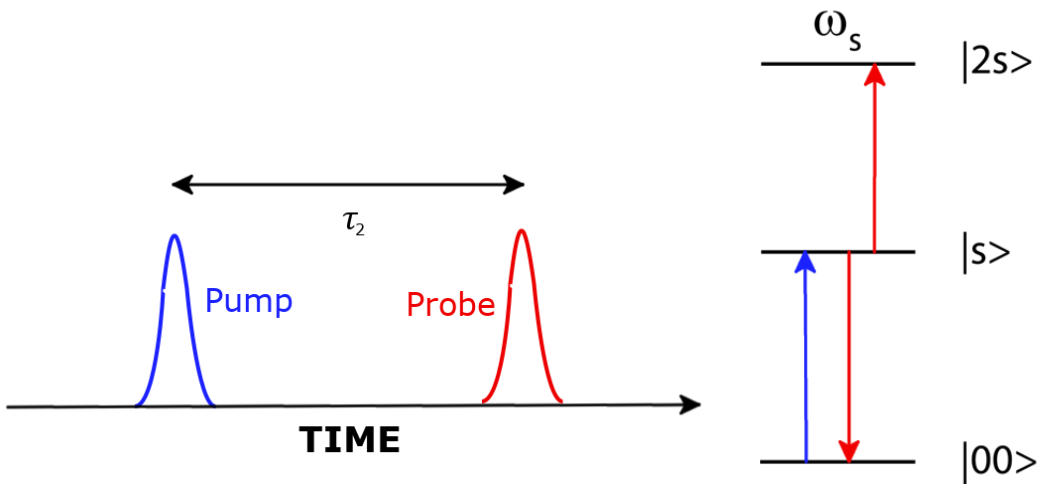

Figure 5.1. PPIR laser pulse diagram (right) and ladder diagram (left). The pump pulse and its effect on the vibrational state of the analyte are pictured in blue, while the probe pulse and its effect on the analyte are shown in red.

5.2 PPIR SEC DATA OF $Fe^{III}(CN)_6^{3-}$

The culmination of all this development is a proof of function – hereafter called a function test. The most simple and reliable test is a pump-probe IR function test. As previously described in this work, this PPIR function test was successfully demonstrated using $Fe^{II\backslash III}(CN)_6^{4-\backslash 3-}$, because both its spectral and electrochemical properties are well-characterized in literature[27,34,35]. The features of greatest interest are the peak frequencies of the excited-state absorption (at $2017cm^{-1}$ for $Fe^{II}(CN)_6^{4-}$ and $2089cm^{-1}$ for $Fe^{III}(CN)_6^{3-}$), ground-state bleach (at $2037cm^{-1}$ for, $Fe^{II}(CN)_6^{4-}$ and $2110cm^{-1}$ for $Fe^{III}(CN)_6^{3-}$) and the excited-state lifetime. The most noteworthy data is displayed in Figure 5.2, Figure 5.3, and Figure 5.4.

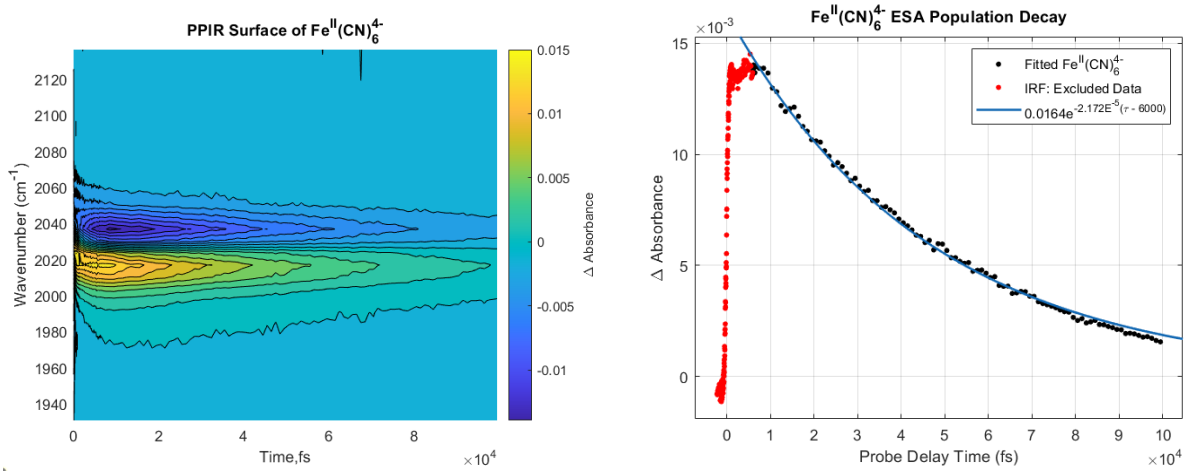

Figure 5.2. PPIR SEC Spectrum of $Fe^{III}(CN)_6^{3-}$ held at 0.0V vs AgCl. (Left) PPIR absorption spectrum surface of a $Fe^{III}(CN)_6^{(3-)}$ in 1M KNO_3 formamide in the SEC cell, with the potential held at 0.0V to entirely reduce the sample to an $Fe^{II}(CN)_6^{4-}$ sample. (Right) Slice of the PPIR spectrum taken from a single detector pixel corresponding to the 2017cm^{-1} frequency, labeled as a dashed white line on the left-side graph, and a numerical fit created with Matlab's Fitting GUI. Red dots are data points of the instrument response function and are excluded from the fit, and the solid line is the single-exponential fit line.

Figure 5.2 shows the raw PPIR signal of a $Fe^{III}(CN)_6^{3-}$ in 1M KNO_3 and formamide solvent and held at 0.0V, thus entirely reduced to $Fe^{II}(CN)_6^{4-}$, with all signal values reported as the change in absorption, $-\log_{10}(1+\frac{\Delta T}{T})$. Each time-delayed point per run is the result of 10 seconds (10000 shots) of averaging, and this graph represents the average four separate runs measured at exact time points. The left is the PPIR plot surface, with a white dashed line demonstrating that the right plot is a one-detector pixel time trace at 2017cm^{-1}. The right plot also includes the one-exponential fit deduced via Matlab's fitting app, as well as which data was not included in the exponential fit as it represents the instrument response function. The extracted decay lifetime for this sample was 46.0ps, which falls within the previously reported margin of error for a previously reported study that was performed in pure formamide[35]. It's notable that this decay lifetime is significantly longer than $Fe^{II}(CN)_6^{4-}$ measured in water[34]. This implies that neither the supporting

electrolyte or the electrochemical infrastructure had any significant effect on the observables of this test, although some samples could experience solvatochromatic changes in the presence of a supporting electrolyte. Ultimately, the signal-to-noise ratio, calculated as $\frac{S}{N} = 10\log_{10}\left(\frac{Peak\ Max - Mean\ Baseline}{RMS\ Noise}\right)$, was 16.56dB. The signal to noise of this measurement has certainly been better in previous work in our lab, but it's not problematic either[31].

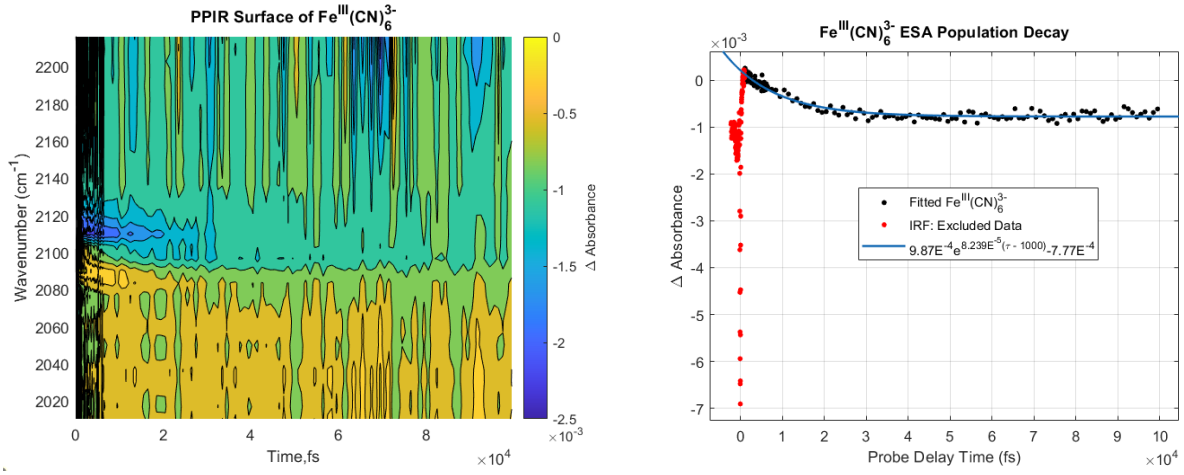

Figure 5.3. PPIR SEC Spectrum of $Fe^{III}(CN)_6^{3-}$ held at 0.4V vs. AgCl. (Left) PPIR absortion spectrum surface of a $Fe^{III}(CN)_6^{3-}$ in 1M KNO_3 formamide in the SEC cell, with the potential held at 0.4V to entirely oxidize the mixed sample of $Fe^{II}(CN)_6^{4-}$ and $Fe^{III}(CN)_6^{3-}$. (Right) Slice of the PPIR spectrum taken from a single detector pixel corresponding to the $2089cm^{-1}$ frequency, labeled as a dashed white line on the left-side graph, and a numerical fit created with Matlab's Fitting GUI. Red dots are data points of the instrument response function and excluded from the fit, and the solid line is the single-exponential fit line.

Figure 5.3 shows the raw PPIR signal of a $Fe^{III}(CN)_6^{3-}$ in 1M KNO_3 and formamide solvent and held at 0.4V, thus entirely oxidizing the mixed sample (from previous experiments) to $Fe^{II}(CN)_6^{4-}$, with all signal values reported as the change in absorption, $-\log_{10}(1+\frac{\Delta T}{T})$. Each time-delayed point per run is the result of 10 seconds (10000 shots) of averaging, and this graph

represents the average four separate runs measured at exact time points. The left is the PPIR plot, with a white dashed line demonstrating that the right plot is a one-pixel time trace at $2089cm^{-1}$. The right plot also includes the one-exponential fit deduced via Matlab's fitting app, as well as which data was not included in the exponential fit as it represents the instrument response function. It's immediately noticeable that the detected difference signal for this $Fe^{II}(CN)_6^{4-}$ is much weaker than the $Fe^{III}(CN)_6^{3-}$ sample, the entire signal is of a comparable magnitude to the noise and scattering experienced from the previous tests. Some of this is expected, as seen in the left of Figure 5.4, the peak amplitude of $Fe^{II}(CN)_6^{4-}$ is generally much weaker than $Fe^{III}(CN)_6^{3-}$. Additionally, previously reported experiments corroborate approximately an order of magnitude less PPIR difference signal in $Fe^{III}(CN)_6^{3-}$ compared to the $Fe^{II}(CN)_6^{4-}$ PPIR signal[34]. It's also worth noting that $Fe^{III}(CN)_6^{3-}$, despite its weak signal, is approximately an order of magnitude more soluble in KNO_3/formamide solution than $Fe^{II}(CN)_6^{4-}$, which is why the $Fe^{III}(CN)_6^{3-}$ sample was preferred for the SEC experiment. The extracted decay lifetime for this sample was 12.1ps, which also falls within the margin of error for a previously reported decay lifetime in pure formamide[35], although in general the literature corroborates that there is less solvatochromatic variance in the PPIR lifetimes of $Fe^{III}(CN)_6^{3-}$ than for $Fe^{II}(CN)_6^{4-}$ [34,35].

Finally, Figure 5.3 also depicts a negative PPIR signal baseline. Given the weakness of this signal, it's possible that this could be a consistent pump beam scattering feature, or it could represent the small signal from extraneous products built up at the surface of the electrode (see Figure 3.11). The former may be more likely, since additional PPIR signal from unexpected RedOx products would not be so broad in spectrum (≈200+cm^{-1} bandwidth, minimum) and such a signal would also feature its own PPIR decay lifetime that is not seen in the time-independent signal offset from this PPIR spectrum surface. Overall, the $\frac{S}{N}$ ratio, calculated the same way as for $Fe^{II}(CN)_6^{4-}$, was

2.58dB – a significant loss and weaker than even 1 minute 2DVE scans in previous work[31]. This being said, the majority of this loss is due to the weak PPIR signal – as the raw quantified RMS noise for the $Fe^{III}(CN)_6^{3-}$ at $8.06 * 10^{-4}$ is of the same magnitude as the $Fe^{II}(CN)_6^{4-}$ RMS noise at $3.34 * 10^{-4}$. This suggests that the scattering between both experiments was actually comparable, but the major distinction was actually in the peak strength over the mean baseline – quantified as 0.015 for the $Fe^{II}(CN)_6^{4-}$ and 0.0015 for $Fe^{III}(CN)_6^{3-}$ - the $Fe^{III}(CN)_6^{3-}$ absorbance signal thus being about 10 times weaker in amplitude than the $Fe^{II}(CN)_6^{4-}$.

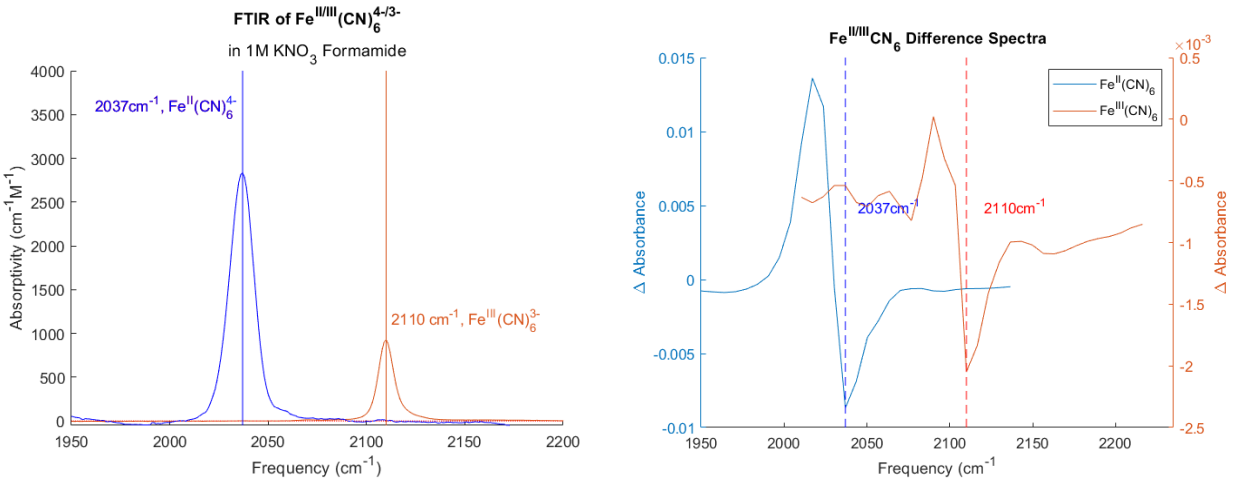

Figure 5.4. FTIR Spectra and PPIR SEC differenc spectra of $Fe^{II\backslash III}(CN)_6^{4-\backslash 3-}$. (Left) FTIR spectra of $Fe^{II}(CN)_6^{4-}$ in blue and $Fe^{III}(CN)_6^{3-}$ in red in KNO_3 formamide, taken with a normal transmissive FTIR spectrometer. (Right) PPIR difference spectra (in ΔA) time slices at τ_2=0 for both $Fe^{II}(CN)_6^{4-}$ in blue and $Fe^{III}(CN)_6^{3-}$ in red in KNO_3 formamide, taken in the SEC cell by holding the potentials at 0.0V and 0.4V vs. AgCl, respectively.

These PPIR spectra alone prove the basic functionality of the SEC cell, albeit perhaps not for weak signals on the same order of magnitude as potential pump scattering. Weaker signals might be better resolved with a wedge-shaped front window for the SEC cell, which could separate the small reflections from the SEC cell front window from the reflection that transmits to the sample.

Additionally, this scattering might have arisen from small scratches to the front window or the ME – the latter of which seems most likely since sample scattering was significantly reduced when the SEC cell was translated such that the IR pump/probe beam focus hit a different part of the ME, suggesting a significant amount of the scattering came from the ME's surface. Since the ME's surface is necessarily made of uncoated Au metal, it's incredibly easy to accidentally scratch the surface, such as attempting to clean the surface. It's also paramount that the BK7 substrate that the Au is sputter coated onto is smooth, as the sputter-coated Au's smoothness will generally reflect the surface it was coated upon. Improving any of these things could reduce detected MIR pump scatter and allow for better resolution of weaker IR signals.

Chapter 6. $Fe^{II\backslash III}(CN)_6^{4-\backslash 3-}$ 2DIR SEC DATA

This chapter begins with a brief tutorial on how to understand and interpret PPIR spectra, then overviews the PPIR SEC experiment as part of the culmination of this work.

6.1 2DIR PRIMER

2DIR, as its name suggests, adds an additional frequency axis to a PPIR measurement – an excitation frequency axis that's labeled as ω_1. As such, 2DIR will share the ground state bleach and excited state absorption features along the detection frequency axis that it shares with PPIR, which is called ω_3 within the context of 2DIR experiments. The ω_3 projections of these spectral difference features will generally mirror the PPIR spectrum and share their underlying causes. However, in the 2D spectra, the original bleach features are now found on the diagonal line of the 2D graph where $\omega_1 = \omega_3$, and the ESA features will be offset in ω_3 just as for the PPIR, but will remain overlapped in the ω_1 projection. These features, and others explained below, are first seen

in Figure 6.1 at $\omega_{a,0}$,$\omega_{a,0}$ and $\omega_{s,0}$,$\omega_{s,0}$ as blue bleach features and orange ESA peaks shifted by Δa and Δs, respectively. Each of these shifts is equal to the difference between the second harmonic of the excited vibrational state and the actual IR resonance that's detected, $\Delta a = 2 * \omega_a - \omega_{2a}$ and $\Delta s = 2 * \omega_s - \omega_{2s}$.

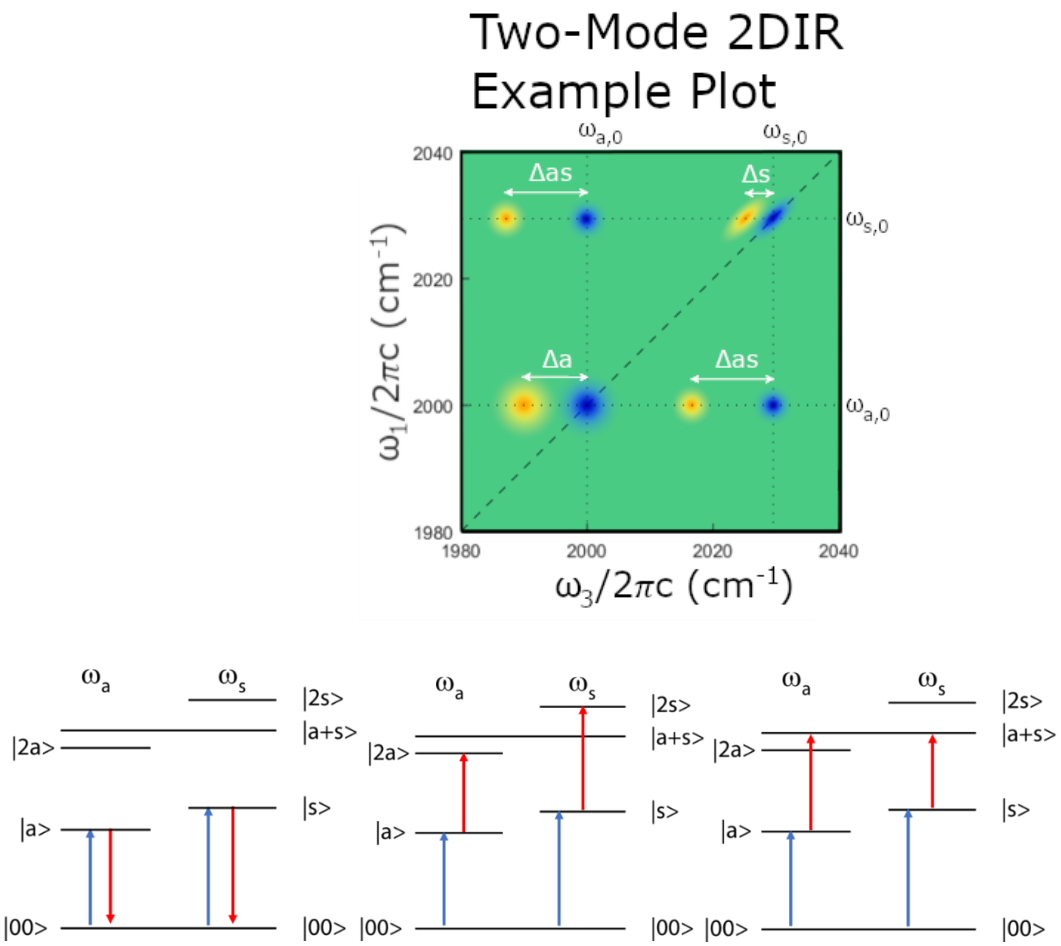

Figure 6.1. Example 2DIR Cartoon. The upper figure is a cartoon 2DIR diagram used to demonstrate a simple, hypothetical 2DIR absorptive spectrum with two ground state vibrations probed in this frequency range, $|a>$ and $|s>$. Increasingly deep blue features are negative in sign, green is zero in sign, and yellow to orange features depict increasingly positive sign values. Below are the 2DIR ladder diagrams that give rise to the features seen in the 2DIR spectrum cartoon. Blue arrows are the net result of the pump beams later seen in Figure 6.2, while the red arrows are the spectral transitions made by the probe beam. The bottom left ladder diagram demonstrates the excited state emission that partially gives rise to the ground state bleach peaks at $\omega_{a,0}, \omega_{a,0}$ and $\omega_{s,0}, \omega_{s,0}$. The bottom middle ladder diagram shows the origins of the excited-state absorption features separated from the anharmonic frequency shifts Δa and Δs, respectively. The bottom right ladder diagram shows the origin of the cross-peak bleach peaks found at $\omega_{a,0}, \omega_{s,0}$ and $\omega_{s,0}, \omega_{a,0}$ and their excited state absorption peaks, both displaced from the bleach feature in ω_3 by Δas.

This new excitation axis, also known as the pump axis or ω_1, is generated from the sample autocorrelation between two pump pulses delayed by a time delay τ_1 before being resolved by the probe pulse delayed by the time τ_2 after the second pump pulse. The autocorrelation of the two pump pulses as a function of τ_1 modulates the measured absorbance signal of the probe, and Fourier-transforming this modulated signal over the τ_1 axis transforms it into the ω_1 axis. The pulse diagram is demonstrated in Figure 6.2. These pump pulses are continuously scanned as part of our previously reported fast-scanning procedure[31] and collected in the same pump-probe geometry used in PPIR experiments – that is to say that the signal is heterodyned into the probe pulse rather than collected separately by making both pump pulse beams colinear.

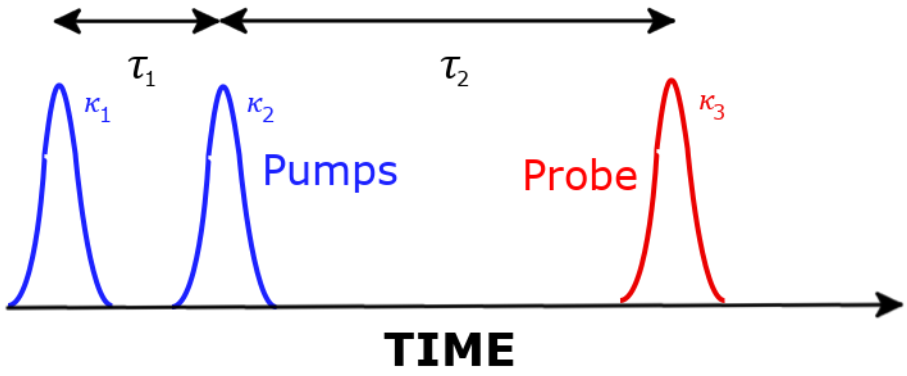

Figure 6.2. Pulse diagram for a typical 2DIR pump-probe geometry experiment. Blue features represent the pump pulses, separated in time by τ_1 and individually labeled with their wave vectors of κ_1 and κ_2. After these pump pulses and separated by a delay time τ_2 is the red probe pulse, labeled with its wave vector κ_3. The pump beams are colinear, so the signal wave vector is $\kappa_1 - \kappa_2 + \kappa_3 = \kappa_3$, being overlapped with the probe pulse.

The ω_1 that distinguishes 2DIR then introduces the possibility of cross-peaks – whose bleach features arise at the confluence of the bleach frequencies of the two original ground state absorption frequencies and seen as the bleach features in Figure 6.1 at $\omega_{a,0}, \omega_{s,0}$ and $\omega_{s,0}, \omega_{a,0}$. These arise from exciting two vibrations being coupled to each other, since exciting one vibration perturbs the other and the energy of exciting both of them will be different than exciting them individually, resulting in an ESA that's red shifted in ω_3 from the cross-peak bleach, seen as the ESA features shifted by Δas from the cross peaks. A larger ESA red shift Δas from the cross-peak bleach directly implies the two vibrational modes being probed are more extensively coupled. Cross peak frequency shifts are quantified as $\Delta as = \omega_{a+s} - (\omega_a + \omega_s)$, i.e. the difference in energy between the combined vibrational state and energy of exciting both vibrational energy states individually. Cross peaks can also be used to assist in resolving convoluted spectra. The amplitude of these peaks is proportional to the angular cross section of the two coupled dipoles, so completely orthogonal dipoles will often have weak cross peaks. Since $Fe^{III}(CN)_6^{3-}$ only features one vibrational mode in this frequency range, cross peaks won't feature in the collected 2DIR spectra in this function test, but will be of great interest during future use of the SEC cell.

The final information of great importance to 2DIR are 2D line shapes. These report to what degree the probed vibration is related to the frequency with which it was pumped. Inhomogenous dephasing (depicted for Figure 6.1's ω_s and Δs feature) means that the excited state vibration interacted with a frequency of light similar to what it was probed with and manifests as a thinner and diagonal 2D line shape. Homogenous dephasing is when we can see that a vibration could be probed by a variety of frequencies very different from the pump frequency and still resonate – that is to say something altered the vibration since it was excited. This manifests as a broad and circular 2D line shape that do not follow the frequency diagonal, which is depicted in Figure 6.1 as the

peaks besides ω_s and Δs. The degree of homogenous vs inhomogenous dephasing reports on the correlation of your vibration to its originally excited state, which will decay at various rates as a function of time between the excitation pump and the probe τ_2. All these 2D line shape phenomena can be analyzed for both diagonal peaks as well as cross-peaks, respectively known as auto and cross correlation. By comparing these line shapes as a function of solvent and time, it's possible to use 2DIR to derive very specific information about how the analyte molecule is solvated[34,36,37].

6.2 2DIR SEC DATA OF $Fe^{III}(CN)_6^{3-}$

While the PPIR SEC test is sufficient to prove the general efficacy of the SEC cell, another goal of this project was to implement 2DIR functionality into our laser table. This was completed, and the first 2DIR SEC function test was completed in our laser lab on the same $Fe^{III}(CN)_6^{3-}$ sample used for the PPIR SEC test. However, as with the PPIR test, the $Fe^{III}(CN)_6^{3-}$ signal was significantly weaker than the $Fe^{II}(CN)_6^{4-}$ signal, and the $Fe^{III}(CN)_6^{3-}$ 2DIR signal is heavily obscured by scattering on the same order of magnitude. Each 2DIR spectrum demonstrated here represents the average two runs, each consisting of ten one-minute 2DIR τ_1 scans consisting of 60,000 detected probe beam shots, half of which are pump-chopped.

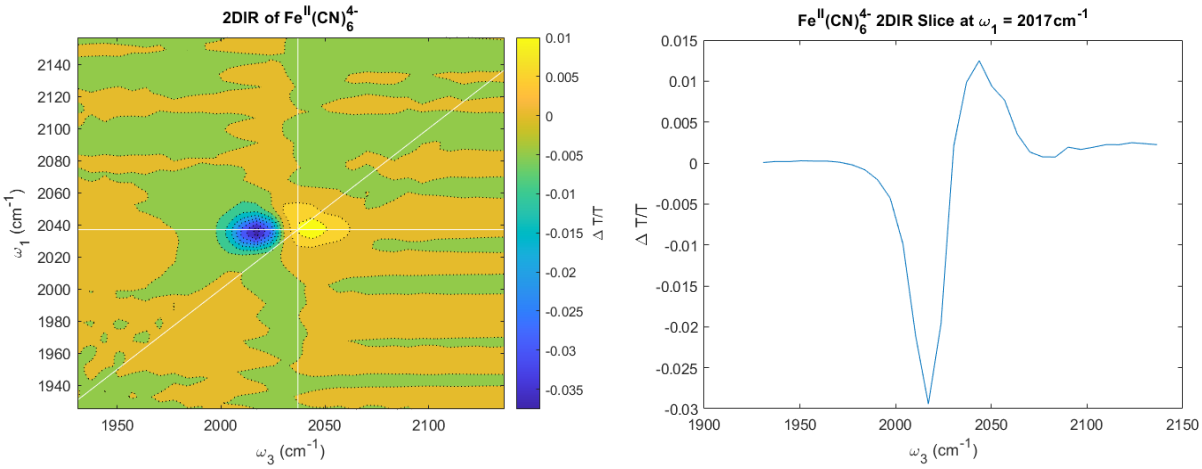

Figure 6.3. 2DIR SEC of $Fe^{III}(CN)_6^{3-}$ held at 0.0V vs AgCl. (Left) Raw 2DIR spectrum of $Fe^{III}(CN)_6^{3-}$ in 1M KNO_3 formamide, with the SEC cell set to 0.0V to convert the entire sample to $Fe^{II}(CN)_6^{4-}$ at τ_2=4.92ps. (Right) 2DIR slice spectra at τ_1=2037cm^{-1}. All signal is reported in $\Delta T/T$.

Figure 6.3 shows the raw 2DIR of the $Fe^{III}(CN)_6^{3-}$ sample held at 0.0V, which reduced the sample to $Fe^{II}(CN)_6^{4-}$. The signal in Figure 37 is reported as the % change in transmission ($\Delta T/T$), and taken at $\tau_2 = 4.92ps$. The signal to noise ratio, as calculated previously, was 2.49dB. This was lower than the PPIR measurement, and possibly due to the degradation of the laser table performance over time. However, this performance is still tenable and prove the collective functionality of the 2DIR and SEC infrastructure. The measured anharmonicity was 14cm^{-1}, calculated by adding the peak shift of the difference spectrum to the raw ω_3 absorption spectrum. This is very close to the $\Delta\nu$ reported for $Fe^{II}(CN)_6^{4-}$ reported previously in pure formamide (16cm^{-1})[35], and is within the difference of one pixel's frequency resolution in this measurement (6.63cm^{-1} between pixels). Overall, these results match previously reported values and demonstrate the efficacy of the SEC cell. Additional frequency precision would simply mean using a different diffraction grating for the spectrometer.

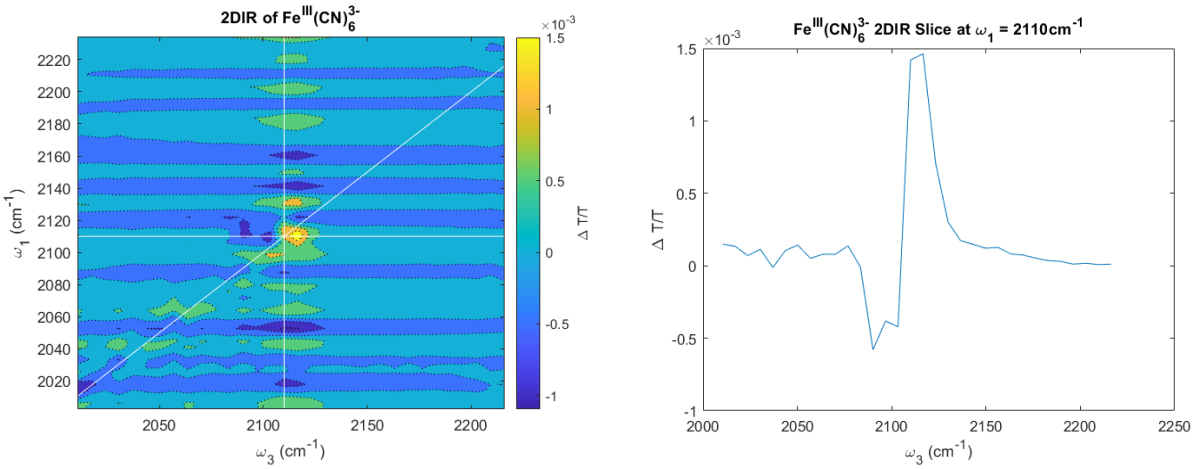

Figure 6.4. 2DIR SEC of $Fe^{III}(CN)_6^{3-}$ held at 0.4V vs AgCl. (Left) Raw 2DIR spectrum at τ_2=4.92ps of $Fe^{III}(CN)_6^{3-}$ in 1M KNO_3 formamide, with the SEC cell set to 0.4V to convert the entire mixed sample of $Fe^{II}(CN)_6^{4-}$ and $Fe^{III}(CN)_6^{3-}$ to $Fe^{III}(CN)_6^{3-}$. (Right) 2DIR slice spectra at τ_1=2110cm^{-1}. All signal reported as $\Delta T/T$.

Figure 6.4 shows the raw 2DIR of the $Fe^{III}(CN)_6^{3-}$ sample held at 0.4V, which ensured full sample oxidation to $Fe^{III}(CN)_6^{3-}$ despite previous experiments resulting in a mixed solution. This signal in Figure 6.4 is reported as the % change in transmission $\Delta T/T$, and taken at $\tau_2 = 4.92ps$. The signal to noise ratio, as calculated previously, was 0.53dB. Considering how much weaker the signal to noise was for the $Fe^{II}(CN)_6$, this shouldn't be a surprise. Just like before, the RMS noise was consistent for both $Fe^{III}(CN)_6^{3-}$ and $Fe^{II}(CN)_6^{4-}$ experiments ($1.84 * 10^{-4}$ and $1.21 * 10^{-4}$, respectively) and the significant difference was purely due to the weaker $Fe^{III}(CN)_6^{3-}$ signal. For these 2DIR plots, the $Fe^{III}(CN)_6^{3-}$ signal is too weak relative to the noise and the 2DIR plot cannot be used for extensive quantitative analysis.

The measured anharmonicity was $7cm^{-1}$, again calculated by adding the peak shift of the difference spectrum to the raw ω_3 absorption spectrum. This is also very close to the $\Delta\nu$ reported for $Fe^{III}(CN)_6^{3-}$ reported previously in pure formamide($16cm^{-1}$)[35], and is still within the

difference of one pixel's frequency resolution in this measurement. Both of these are significantly larger than the $\Delta\nu$ previously reported for PPIR in pure formamide ($9cm^{-1}$)[35], and once again show that this SEC cell infrastructure can reliably replicate previously reported results.

As previously mentioned, the extremely weak $Fe^{III}(CN)_6^{3-}$ difference signal is obscured by the significant pump beam scattering which manifests as ringing in the τ_1/ω_1 axis. This effect is very similar to the result of the ringing observed in the $Fe^{III}(CN)_6^{3-}$ PPIR spectrum's τ_2-dependant ringing. In order to better resolve the $Fe^{III}(CN)_6^{3-}$ 2DIR features, a Savitsky-Golay filter can be applied across the ω_1 axis. The resulting 2DIR spectrum is shown in Figure 6.5, and demonstrates improved visibility of the $Fe^{III}(CN)_6^{3-}$ signal once the ringing in ω_1 is smoothed out. This does come at a detriment to peak location as the smoothing over ω_1 distorts the peak linewidths, and in this case also changes the excited state absorption's peak location on the ω_1 axis, resulting in the peaks no longer being appropriately aligned in ω_1. While this filter helps prove the existence of the $Fe^{III}(CN)_6^{3-}$ signal and the SEC cell's complete conversion of the mixed $Fe^{II\backslash III}(CN)_6^{4-\backslash 3-}$ sample into purely $Fe^{III}(CN)_6^{3-}$, the filter also belies any quantitative analysis that might be done on the resulting spectrum. In order to perform any quantitative analysis on this 2DIR spectrum, as was the case for the similar PPIR spectrum, the pump beam scattering to the MCMCT detector must be significantly reduced via smoother ME and front window surfaces.

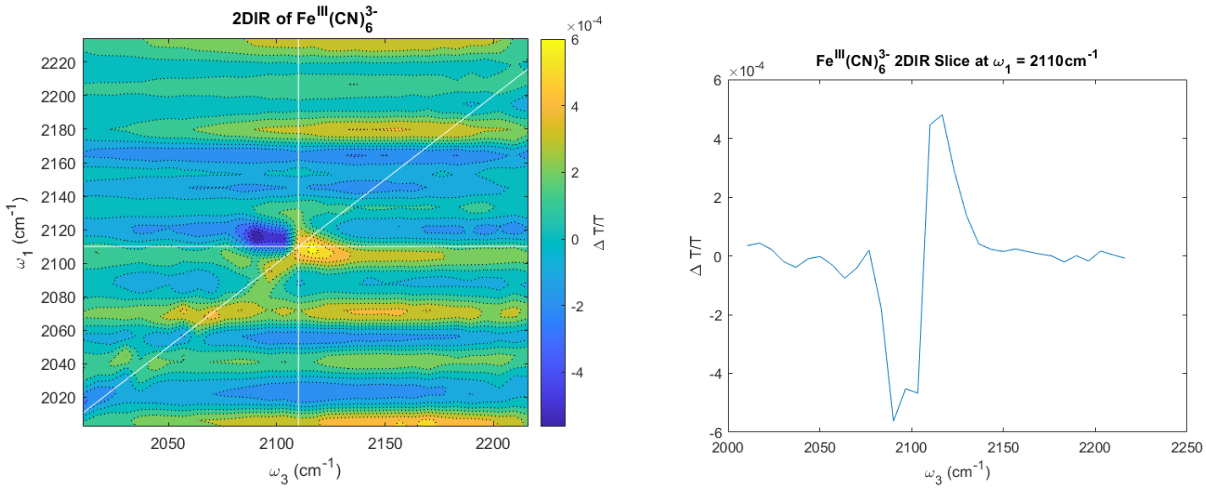

Figure 6.5. 2DIR SEC of $Fe^{III}(CN)_6^{3-}$ held at 0.4V vs AgCl, SG Filtered. (Left) Raw 2DIR spectrum at τ_2=0 of $Fe^{III}(CN)_6^{3-}$ in 1M KNO_3 formamide, with the SEC cell set to 0.4V vs AgCl to convert the entire mixed sample of $Fe^{II}(CN)_6^{4-}$ and $Fe^{III}(CN)_6^{3-}$ to $Fe^{III}(CN)_6^{3-}$. A Savitzky-Golay frequency filter with an 8 point window across τ_1 is applied to the spectrum to help visualize the $Fe^{III}(CN)_6^{3-}$ peaks. (Right) 2DIR slice spectra at τ_1=2110cm^{-1} All signal is reported as $\Delta T/T$.

While the weak $Fe^{III}(CN)_6^{3-}$ 2DIR and PPIR spectra make any precise quantitative analysis somewhat spurious, the 2DIR and PPIR SEC spectra match previously reported analysis of $Fe^{(II)(CN)_6^{4-}}$ and $Fe^{(III)(CN)_6^{3-}}$ within the experimental precision limited by the laser table infrastructure used. Additional precision could be calculated in the future by using a different diffraction grating, as well as performing the ultrafast experiments in a shorter time frame to avoid performance losses as laser table alignment slowly falls. This, as well as reducing scattering by using fresh window pieces and unscratched ME's, are absolutely necessary in order to detect weaker spectral features like the $Fe^{III}(CN)_6^{3-}$, but the only unique challenge presented by this compared to normal ultrafast experiments is the ME.

6.3 REFERENCES

1. Chikkaveeraiah, B. V., Bhirde, A. A., Morgan, N. Y., Eden, H. S. & Chen, X. Electrochemical immunosensors for detection of cancer protein biomarkers. *ACS Nano* **6**, 6546–6561 (2012).
2. Myamlin, V. A. & Pleskov, Y. V. Electrochemistry of Semiconductors. *Electrochem. Semicond.* **3**, 87–91 (1967).
3. Oja, S. M., Fan, Y., Armstrong, C. M., Defnet, P. & Zhang, B. Nanoscale Electrochemistry Revisited. *Anal. Chem.* **88**, 414–430 (2016).
4. Kuwana, T., Darlington, R. K. & Leedy, D. W. Electrochemical Studies Using Conducting Glass Indicator Electrodes. *Anal. Chem.* **36**, 2023–2025 (1964).
5. Flowers, P. A. & Mamantov, G. Thin-Layer Transmittance Cell for Infrared Spectroelectrochemistry. *Anal. Chem.* **61**, 190–192 (1989).
6. Smieja, J. M. & Kubiak, C. P. Re(bipy-tBu)(CO)3Cl-improved catalytic activity for reduction of carbon dioxide: IR-spectroelectrochemical and mechanistic studies. *Inorg. Chem.* **49**, 9283–9289 (2010).
7. Machan, C. W., Sampson, M. D., Chabolla, S. A., Dang, T. & Kubiak, C. P. Developing a mechanistic understanding of molecular electrocatalysts for CO2 reduction using infrared spectroelectrochemistry. *Organometallics* **33**, 4550–4559 (2014).
8. Porter, T. M., Heim, G. P. & Kubiak, C. P. Stable Mixed-Valent Complexes Formed by Electron Delocalization Across Hydrogen Bonds of Pyrimidinone-Linked Metal Clusters. *J. Am. Chem. Soc.* jacs.8b09273 (2018) doi:10.1021/jacs.8b09273.
9. Kiefer, L. M., Michocki, L. B. & Kubarych, K. J. Transmission Mode 2D-IR Spectroelectrochemistry of In Situ Electrocatalytic Intermediates. *J. Phys. Chem. Lett.*

3712–3717 (2021) doi:10.1021/acs.jpclett.1c00504.

10. Zhai, Y., Zhu, Z., Zhou, S., Zhu, C. & Dong, S. Recent advances in spectroelectrochemistry. *Nanoscale* **10**, 3089–3111 (2018).
11. Kaim, W. & Fiedler, J. Spectroelectrochemistry: The best of two worlds. *Chem. Soc. Rev.* **38**, 3373–3382 (2009).
12. Durliat, H. & Comtat, M. Investigation of Electron Transfer between Platinum and Large Biological Molecules by Thin-Layer Spectroelectrochemistry. *Anal. Chem.* **54**, 856–861 (1982).
13. Rosser, T. E. & Reisner, E. Understanding Immobilized Molecular Catalysts for Fuel-Forming Reactions through UV/Vis Spectroelectrochemistry. *ACS Catal.* **7**, 3131–3141 (2017).
14. Trznadel, M. *et al.* UV-VIS-NIR and Raman spectroelectrochemistry of regioregular poly(3-octylthiophene): Comparison with its non-regioregular analogue. *J. Chem. Soc. - Faraday Trans.* **92**, 1387–1393 (1996).
15. El Khoury, Y., van wilderen, L. J. G. W., Vogt, T., Winter, E. & Bredenbeck, J. A spectroelectrochemical cell for ultrafast two-dimensional infrared spectroscopy. *Rev. Sci. Instrum.* **86**, (2015).
16. Heitmüller, J. *et al.* Coherent two-dimensional electronic spectroelectrochemistry. *Spectrochim. Acta - Part A Mol. Biomol. Spectrosc.* **253**, 119567 (2021).
17. Weppner, W. & Huggins, R. A. Electrochemical methods for determining kinetic properties of solids. *Annu. Rev. Mater. Sci.* **8**, 269–311 (1978).
18. Durst, J. *et al.* New insights into the electrochemical hydrogen oxidation and evolution reaction mechanism. *Energy Environ. Sci.* **7**, 2255–2260 (2014).

19. Pieslinger, G. E., Albores, P., Slep, L. D. & Baraldo, L. M. Class III delocalization in a cyanide-bridged trimetallic mixed-valence complex. *Angew. Chemie - Int. Ed.* **53**, 1293–1296 (2014).

20. Oviedo, P. S., Pieslinger, G. E., Cadranel, A. & Baraldo, L. M. Exploring the localized to delocalized transition in non-symmetric bimetallic ruthenium polypyridines. *Dalt. Trans.* **46**, 15757–15768 (2017).

21. Lotti, D., Hamm, P. & Kraack, J. P. Surface-Sensitive Spectro-electrochemistry Using Ultrafast 2D ATR IR Spectroscopy. *J. Phys. Chem. C* **120**, 2883–2892 (2016).

22. Kraack, J. P. & Hamm, P. Surface-Sensitive and Surface-Specific Ultrafast Two-Dimensional Vibrational Spectroscopy. *Chem. Rev.* **117**, 10623–10664 (2017).

23. Kraack, J. P., Kaech, A. & Hamm, P. Surface Enhancement in Ultrafast 2D ATR IR Spectroscopy at the Metal-Liquid Interface. *J. Phys. Chem. C* **120**, 3350–3359 (2016).

24. El Khoury, Y., Van Wilderen, L. J. G. W. & Bredenbeck, J. Ultrafast 2D-IR spectroelectrochemistry of flavin mononucleotide. *J. Chem. Phys.* **142**, 212416 (2015).

25. Parker, D. *et al.* Polymers, High-Temperature. *Ullmann's Encyclopedia of Industrial Chemistry* (2012) doi:https://doi.org/10.1002/14356007.a21_449.pub4.

26. Dobbelaere, T., Vereecken, P. M. & Detavernier, C. A USB-controlled potentiostat/galvanostat for thin-film battery characterization. *HardwareX* **2**, 34–49 (2017).

27. Ross, M. *et al.* Comprehensive Experimental and Computational Spectroscopic Study of Hexacyanoferrate Complexes in Water: From Infrared to X-ray Wavelengths. *J. Phys. Chem. B* **122**, 5075–5086 (2018).

28. Weidinger, D., Sando, G. M. & Owrutsky, J. C. Vibrational dynamics of metal cyanides.

Chem. Phys. Lett. **489**, 169–174 (2010).

29. Rooney, M. B., Coomber, D. C. & Bond, A. M. Achievement of near-reversible behavior for the [Fe(CN)6]3-/4- Redox couple using cyclic voltammetry at glassy carbon, gold, and platinum macrodisk electrodes in the absence of added supporting electrolyte. *Anal. Chem.* **72**, 3486–3491 (2000).
30. Bard, A. J. & Faulkner, L. R. *Electrochemical Methods: Fundamentals and Applications*. (John Wiley and Sons, Inc., 2001).
31. Fox, Z. W., Blair, T. J., Weakly, R. B., Courtney, T. L. & Khalil, M. Implementation of continuous fast scanning detection in femtosecond Fourier-transform two-dimensional vibrational-electronic spectroscopy to decrease data acquisition time. *Rev. Sci. Instrum.* **89**, (2018).
32. Middleton, C. T., Woys, A. M., Mukherjee, S. S. & Zanni, M. T. Residue-specific structural kinetics of proteins through the union of isotope labeling, mid-IR pulse shaping, and coherent 2D IR spectroscopy. *Methods* **52**, 12–22 (2010).
33. Banno, M., Ohta, K., Yamaguchi, S., Hirai, S. & Tominaga, K. Vibrational Dynamics of Hydrogen-Bonded Complexes in Solutions Studied with Ultrafast Infrared Pump−Probe Spectroscopy. *Acc. Chem. Res.* **42**, 1259–1269 (2009).
34. Yu, P., Yang, F., Zhao, J. & Wang, J. Hydration dynamics of cyanoferrate anions examined by ultrafast infrared spectroscopy. *J. Phys. Chem. B* **118**, 3104–3114 (2014).
35. Sando, G. M. *et al.* Vibrational and rotational dynamics of cyanoferrates in solution Vibrational and rotational dynamics of cyanoferrates in solution. *J. Chem. Phys.* **121**, 2158–2168 (2004).
36. Kiefer, L. M. & Kubarych, K. J. Solvent- - - Dependent Dynamics of a Series of Rhenium

Photo- - - Activated Catalysts Measured with Ultrafast 2DIR lar Aprotic Solvents S3 . DFT Calculated Carbonyl Vibrational Stretching Frequencies and Partial Charges of. **3**,.

37. Kiefer, L. M. & Kubarych, K. J. Solvent exchange in preformed photocatalyst- donor precursor complexes determines efficiency. *Chem. Sci.* **9**, 1527–1533 (2018).

VITA

William Miller was born in Ann Arbor, MI. in 1993 and grew up in Saline, MI. He graduated from Saline Public High School in 2012 and played American football, rugby, and wrestled. William attended the University of Michigan (Ann Arbor) from 2012- 2016 and took a couple years before deciding to major in chemistry. During this time, he also worked as an ambulance EMS provider in Wayne County, MI. He graduated from the University of Michigan with Bachelor of Science degree in Chemistry. In Autumn 2017, William entered the Ph.D. program in Chemistry at the University of Washington and joined the research group of Professor Munira Khalil. It was during this time, William's depression hit an all-time low from 2018-2019, but he rebounded during the COVID-19 epidemic of 2020 after gaining a much deeper relationship with his friends and meeting his current partner, Alyssa Rehwald. In June 2023, William completed his Doctor of Philosophy degree in Chemistry. He will take some much-needed rest over the summer, during which time he'll also begin a career in education either in a public primary school or a teaching college in the Seattle area. William is an insatiable foodie with a love of history and geeky hobbies.